The DECam Local Volume Exploration Survey Data Release 2

```
A. Drlica-Wagner ©, 1, 2, 3 P. S. Ferguson ®, 4 M. Adamów ®, 5 M. Aguena, 6 S. Allam, 1 F. Andrade-Oliveira, 7 D. Bacon, 8 K. Bechtol ®, 4 E. F. Bell ®, 9 E. Bertin, 10, 11 P. Bilaji, 2, 12 S. Bocquet ®, 13 C. R. Bom ®, 14 D. Brooks ®, 15 D. L. Burke, 16, 17 J. A. Carballo-Bello ®, 18 J. L. Carlin ®, 19 A. Carrero Rosell ®, 20, 6, 21 M. Carrasco Kind ®, 5, 22 J. Carretreo ®, 23 F. J. Castander ®, 24, 25 W. Cerny ®, 2, 3 C. Chang ®, 3, 2 Y. Chol, 26 C. Conselice ®, 27, 28 M. Costanzi, 29, 30, 31 D. Crrojevic ®, 32 L. N. da Costa, 6, 33 J. De Vicente ®, 34 S. Desai ®, 35 J. Esteves, 7 S. Everett, 36 I. Ferrero, 37 M. Fitzpatrick ®, 38 B. Flaugher ®, 1 D. Frieddel, 5 J. Frieman ®, 3, 2, 1 J. García-Belldo ®, 39 M. Gatti, 40 E. Gaztanaga ®, 24, 25 D. W. Gerdes ®, 41, 7 D. Gruen ®, 13 R. A. Gruendl ®, 5, 22, 42 J. Gschwend ®, 6, 33 W. G. Hartley, 43 D. Hernandez-Lang, 44 S. R. Hinton, 45 D. L. Hollowood, 36 K. Honscheid ®, 46, 47 A. K. Hughes, 48 A. Jacques ®, 38 D. J. James ®, 49 M. D. Johnson, 5 K. Kuehn ®, 50, 51 N. Kuropatkin, 1 O. Lahav ®, 15 T. S. Li ®, 2 C. Lidman ®, 53, 54 H. Lin ®, 1 M. March, 40 J. L. Marshall ®, 55 D. Martínez-Delgado ®, 66 C. E. Martínez-Vázquez ®, 57, 58 P. Massana ®, 59 S. Mau ®, 60, 16 M. McNana ®, 4 P. Melchior ®, 61 F. Menanteau ®, 5, 22 A. E. Miller ®, 62, 63 R. Miquel ®, 64, 23 J. J. Mohr, 65, 13 R. Morgan, 4 B. Mutlu-Pakdil, 2, 3 R. R. Muñoz ®, 66 E. H. Neilsen ®, 61, 10 L. Nidever, 59, 38 R. Nikutta ®, 38 J. L. Nilo Castellon, 67, 68 N. E. D. Noël, 69 R. L. C. Ogando ®, 33 K. A. G. Olsen, 38 A. B. Pace ®, 70 A. Palmese ®, 71 F. Paz-Chinchón, 5, 72 M. E. S. Pereira, 73 A. Pieres ®, 6, 33 A. A. Plazas Malagón ®, 61 J. Prat, 3, 2 A. H. Riley, 55 M. Rodriguez-Monroy, 74 A. K. Romer ®, 75 A. Roodman ®, 16, 17 M. Sako, 40 J. D. Sakowska ®, 69 E. Sanchez ®, 34 F. J. Sánchez ®, 1 D. J. Sand ®, 48 L. Santana-Silva, 76 B. Santiago, 77, 6 M. Schubrell ®, 7 S. Serrano, 24, 25 L. Sevilla-Noarbe ®, 41 D. Simon ®, 82 C. Y. Tan ®, 2, 12 G. Tarle ®, 7 K. Tavangar, 83, 3 D. Thomas, 8 C. To ®, 46
```

```
<sup>1</sup>Fermi National Accelerator Laboratory, P.O. Box 500, Batavia, IL 60510, USA
                      <sup>2</sup> Kavli Institute for Cosmological Physics, University of Chicago, Chicago, IL 60637, USA
                   <sup>3</sup>Department of Astronomy and Astrophysics, University of Chicago, Chicago, IL 60637, USA
<sup>4</sup> Physics Department, 2320 Chamberlin Hall, University of Wisconsin-Madison, 1150 University Avenue Madison, WI 53706-1390
<sup>5</sup>Center for Astrophysical Surveys, National Center for Supercomputing Applications, 1205 West Clark St., Urbana, IL 61801, USA
   <sup>6</sup> Laboratório Interinstitucional de e-Astronomia - LIneA, Rua Gal. José Cristino 77, Rio de Janeiro, R.J. - 20921-400, Brazil
                            <sup>7</sup>Department of Physics, University of Michigan, Ann Arbor, MI 48109, USA
                   <sup>8</sup> Institute of Cosmology and Gravitation, University of Portsmouth, Portsmouth, PO1 3FX, UK
            Department of Astronomy, University of Michigan, 1085 S. University Ave., Ann Arbor, 48109-1107, USA
                           <sup>10</sup>CNRS, UMR 7095, Institut d'Astrophysique de Paris, F-75014, Paris, France
       <sup>11</sup>Sorbonne Universités, UPMC Univ Paris 06, UMR 7095, Institut d'Astrophysique de Paris, F-75014, Paris, France
                              <sup>12</sup>Department of Physics, University of Chicago, Chicago, IL 60637, USA
      <sup>13</sup> University Observatory, Faculty of Physics, Ludwig-Maximilians-Universität, Scheinerstr. 1, 81679 Munich, Germany
            <sup>14</sup>Centro Brasileiro de Pesquisas Físicas, Rua Dr. Xavier Sigaud 150, 22290-180 Rio de Janeiro, RJ, Brazil
            <sup>15</sup>Department of Physics & Astronomy, University College London, Gower Street, London, WC1E 6BT, UK
     <sup>16</sup>Kavli Institute for Particle Astrophysics & Cosmology, P.O. Box 2450, Stanford University, Stanford, CA 94305, USA
                               <sup>17</sup>SLAC National Accelerator Laboratory, Menlo Park, CA 94025, USA
   <sup>18</sup> Instituto de Alta Investigación, Sede Esmeralda, Universidad de Tarapacá, Av. Luis Emilio Recabarren 2477, Iquique, Chile
                         <sup>19</sup>Rubin Observatory/AURA, 950 North Cherry Avenue, Tucson, AZ, 85719, USA
                             <sup>20</sup>Instituto de Astrofisica de Canarias, E-38205 La Laguna, Tenerife, Spain
                        <sup>21</sup> Universidad de La Laguna, Dpto. Astrofísica, E-38206 La Laguna, Tenerife, Spain
     <sup>22</sup>Department of Astronomy, University of Illinois at Urbana-Champaign, 1002 W. Green Street, Urbana, IL 61801, USA
```

Corresponding author: Alex Drlica-Wagner (kadrlica@fnal.gov), Peter Ferguson (peter.ferguson@wisc.edu)

```
<sup>23</sup> Institut de Física d'Altes Energies (IFAE), The Barcelona Institute of Science and Technology, Campus UAB, 08193 Bellaterra
                                                               (Barcelona) Spain
                                <sup>24</sup>Institut d'Estudis Espacials de Catalunya (IEEC), 08034 Barcelona, Spain
            <sup>25</sup>Institute of Space Sciences (ICE, CSIC), Campus UAB, Carrer de Can Magrans, s/n, 08193 Barcelona, Spain
                         <sup>26</sup>Space Telescope Science Institute, 3700 San Martin Drive, Baltimore, MD 21218, USA
  <sup>27</sup> Jodrell Bank Center for Astrophysics, School of Physics and Astronomy, University of Manchester, Oxford Road, Manchester, M13
                        <sup>28</sup> University of Nottingham, School of Physics and Astronomy, Nottingham NG7 2RD, UK
                  <sup>29</sup> Astronomy Unit, Department of Physics, University of Trieste, via Tiepolo 11, I-34131 Trieste, Italy
                         <sup>30</sup>INAF-Osservatorio Astronomico di Trieste, via G. B. Tiepolo 11, I-34143 Trieste, Italy
                          <sup>31</sup>Institute for Fundamental Physics of the Universe, Via Beirut 2, 34014 Trieste, Italy
         <sup>32</sup>Department of Chemistry and Physics, University of Tampa, 401 West Kennedy Boulevard, Tampa, FL 33606, USA
                       <sup>33</sup> Observatório Nacional, Rua Gal. José Cristino 77, Rio de Janeiro, RJ - 20921-400, Brazil
                  <sup>34</sup> Centro de Investigaciones Energéticas, Medioambientales y Tecnológicas (CIEMAT), Madrid, Spain
                                 <sup>35</sup>Department of Physics, IIT Hyderabad, Kandi, Telangana 502285, India
                                 <sup>36</sup>Santa Cruz Institute for Particle Physics, Santa Cruz, CA 95064, USA
               <sup>37</sup> Institute of Theoretical Astrophysics, University of Oslo. P.O. Box 1029 Blindern, NO-0315 Oslo, Norway
            <sup>38</sup> NSF's National Optical-Infrared Astronomy Research Laboratory, 950 N. Cherry Ave., Tucson, AZ 85719, USA
                    <sup>39</sup>Instituto de Fisica Teorica UAM/CSIC, Universidad Autonoma de Madrid, 28049 Madrid, Spain
                   <sup>40</sup>Department of Physics and Astronomy, University of Pennsylvania, Philadelphia, PA 19104, USA
                             <sup>41</sup>Department of Astronomy, University of Michigan, Ann Arbor, MI 48109, USA
                    <sup>42</sup> National Center for Supercomputing Applications, 1205 West Clark St., Urbana, IL 61801, USA
                    <sup>43</sup>Department of Astronomy, University of Geneva, ch. d'Écoqia 16, CH-1290 Versoix, Switzerland
                      <sup>44</sup> Faculty of Physics, Ludwig-Maximilians-Universität, Scheinerstr. 1, 81679 Munich, Germany
                     <sup>45</sup>School of Mathematics and Physics, University of Queensland, Brisbane, QLD 4072, Australia
               <sup>46</sup>Center for Cosmology and Astro-Particle Physics. The Ohio State University, Columbus, OH 43210, USA
                             <sup>47</sup>Department of Physics, The Ohio State University, Columbus, OH 43210, USA
        <sup>48</sup>Department of Astronomy/Steward Observatory, 933 North Cherry Avenue, Room N204, Tucson, AZ 85721-0065, USA
                                         <sup>49</sup> ASTRAVEO LLC. PO Box 1668. Gloucester. MA 01931
                       <sup>50</sup> Australian Astronomical Optics, Macquarie University, North Ryde, NSW 2113, Australia
                                    <sup>51</sup>Lowell Observatory, 1400 Mars Hill Rd, Flagstaff, AZ 86001, USA
      <sup>52</sup>Department of Astronomy and Astrophysics, University of Toronto, 50 St. George Street, Toronto ON, M5S 3H4, Canada
         <sup>53</sup> Centre for Gravitational Astrophysics, College of Science, The Australian National University, ACT 2601, Australia
               <sup>54</sup> The Research School of Astronomy and Astrophysics, Australian National University, ACT 2601, Australia
<sup>55</sup>George P. and Cynthia Woods Mitchell Institute for Fundamental Physics and Astronomy, and Department of Physics and Astronomy,
                                           Texas A&M University, College Station, TX 77843, USA
                                  <sup>56</sup>Instituto de Astrofísica de Andalucía, CSIC, E-18080 Granada, Spain
 <sup>57</sup> Gemini Observatory, NSF's National Optical-Infrared Astronomy Research Laboratory, 670 N. A'ohoku Place, Hilo, HI 96720, USA
 <sup>58</sup> Cerro Tololo Inter-American Observatory, NSF's National Optical-Infrared Astronomy Research Laboratory, Casilla 603, La Serena,
                    <sup>59</sup>Department of Physics, Montana State University, P.O. Box 173840, Bozeman, MT 59717-3840
                      <sup>60</sup>Department of Physics, Stanford University, 382 Via Pueblo Mall, Stanford, CA 94305, USA
                  <sup>61</sup>Department of Astrophysical Sciences, Princeton University, Peyton Hall, Princeton, NJ 08544, USA
                  <sup>62</sup>Leibniz-Institut für Astrophysik Potsdam (AIP), An der Sternwarte 16, D-14482 Potsdam, Germany
<sup>63</sup> Institut für Physik und Astronomie, Universität Potsdam, Haus 28, Karl-Liebknecht-Str. 24/25, D-14476 Golm (Potsdam), Germany
                              <sup>64</sup>Institució Catalana de Recerca i Estudis Avançats, E-08010 Barcelona, Spain
                    <sup>65</sup>Max Planck Institute for Extraterrestrial Physics, Giessenbachstrasse, 85748 Garching, Germany
           <sup>66</sup>Departamento de Astronomía, Universidad de Chile, Camino El Observatorio 1515, Las Condes, Santiago, Chile
               <sup>67</sup>Departamento de Astronomía, Universidad de La Serena, Avenida Juan Cisternas 1200, La Serena, Chile
        <sup>68</sup> Dirección de Investigación y Desarrollo, Universidad de La Serena, Av. Raúl Bitrán Nachary N. 1305, LaSerena, Chile
                                  <sup>69</sup>Department of Physics, University of Surrey, Guildford GU2 7XH, UK
             <sup>70</sup>McWilliams Center for Cosmology, Carnegie Mellon University, 5000 Forbes Ave, Pittsburgh, PA 15213, USA
             <sup>71</sup>Department of Astronomy, University of California, Berkeley, 501 Campbell Hall, Berkeley, CA 94720, USA
                      <sup>72</sup>Institute of Astronomy, University of Cambridge, Madingley Road, Cambridge CB3 0HA, UK
                      <sup>73</sup> Hamburger Sternwarte, Universität Hamburg, Gojenbergsweg 112, 21029 Hamburg, Germany
<sup>74</sup>Laboratoire de physique des 2 infinis Irène Joliot-Curie, CNRS Université Paris-Saclay, Bât. 100, Faculté des sciences, F-91405 Orsay
```

Cedex, France

75 Department of Physics and Astronomy, Pevensey Building, University of Sussex, Brighton, BN1 9QH, UK
 76 NAT-Universidade Cruzeiro do Sul / Universidade Cidade de São Paulo, Rua Galvão Bueno, 868, 01506-000, São Paulo, SP, Brazil
 77 Instituto de Física, UFRGS, Caixa Postal 15051, Porto Alegre, RS - 91501-970, Brazil
 78 Observatories of the Carnegie Institution for Science, 813 Santa Barbara St., Pasadena, CA 91101, USA
 79 School of Physics and Astronomy, University of Southampton, Southampton, SO17 1BJ, UK
 80 Center for Astrophysics and Space Astronomy, University of Colorado, 389 UCB, Boulder, CO 80309-0389, USA
 81 Computer Science and Mathematics Division, Oak Ridge National Laboratory, Oak Ridge, TN 37831
 82 Department of Chemistry and Physics, Purdue University Northwest, Hammond, IN 46323, USA
 83 Center for Computational Astrophysics, Flatiron Institute, Simons Foundation, 162 Fifth Avenue, New York, NY 10010, USA
 84 Department of Physics, Duke University Durham, NC 27708, USA
 85 Excellence Cluster Origins, Boltzmannstr. 2, 85748 Garching, Germany
 86 Universitäts-Sternwarte, Fakultät für Physik, Ludwig-Maximilians Universität München, Scheinerstr. 1, 81679 München, Germany

ABSTRACT

We present the second public data release (DR2) from the DECam Local Volume Exploration survey (DELVE). DELVE DR2 combines new DECam observations with archival DECam data from the Dark Energy Survey, the DECam Legacy Survey, and other DECam community programs. DELVE DR2 consists of $\sim 160,000$ exposures that cover $> 21,000\,\mathrm{deg^2}$ of the high Galactic latitude ($|b| > 10\,\mathrm{deg}$) sky in four broadband optical/near-infrared filters (g,r,i,z). DELVE DR2 provides point-source and automatic aperture photometry for ~ 2.5 billion astronomical sources with a median 5σ point-source depth of $g{=}24.3,\ r{=}23.9,\ i{=}23.5,\ \mathrm{and}\ z{=}22.8$ mag. A region of $\sim 17,000\,\mathrm{deg^2}$ has been imaged in all four filters, providing four-band photometric measurements for ~ 618 million astronomical sources. DELVE DR2 covers more than four times the area of the previous DELVE data release and contains roughly five times as many astronomical objects. DELVE DR2 is publicly available via the NOIRLab Astro Data Lab science platform.

Keywords: Surveys – Catalogs

1. INTRODUCTION

Digital sky surveys at optical/near-infrared wavelengths have revolutionized astronomy. These large, untargeted observational programs provide expansive data sets that enable unprecedented statistical studies and fortuitous discoveries across a wide range of astronomical fields. The Sloan Digital Sky Survey (SDSS; York et al. 2000), the Two Micron All-Sky Survey (2MASS Skrutskie et al. 2006), the Pan-STARRS1 survey (PS1; Chambers et al. 2016), and the SkyMapper Southern Sky Survey (Wolf et al. 2018) have provided an unprecedented view of the sky. However, these surveys were carried out on relatively small ($\lesssim 2.5$ -m diameter) telescopes, which limited their sensitivity, especially in the southern hemisphere.

The 570-megapixel Dark Energy Camera (DECam; Flaugher et al. 2015) on the 4-m Victor M. Blanco Telescope at Cerro Tololo in Chile is the premier optical/near-infrared survey instrument in the southern hemisphere. Since commissioning in 2012, DECam has been used by the Dark Energy Survey (DES; DES Collaboration 2005, 2016), the DECam Legacy Survey (DECaLS; Dey et al. 2019), and numerous smaller com-

munity programs. Through these programs, DECam has gradually, and somewhat unsystematically, imaged much of the southern celestial hemisphere (e.g., Nidever et al. 2021). The DECam Local Volume Exploration Survey (DELVE; Drlica-Wagner et al. 2021)¹ seeks to complete contiguous DECam coverage of the southern sky by selectively observing regions of the sky that lack existing observations. The primary science goals of DELVE are to discover and characterize faint satellite galaxies and other resolved stellar systems around the Milky Way, Magellanic Clouds, and isolated Magellanic analogs in the Local Volume (Drlica-Wagner et al. 2021). The DELVE science program has already resulted in the discovery and characterization of five ultra-faint Milky Way satellites (Mau et al. 2020; Martínez-Vázquez et al. 2021; Cerny et al. 2021a,b, 2022) and an extended study of the Jet stellar stream (Ferguson et al. 2022). Moreover, the unprecedented wide, deep DELVE data set has broad applicability to a wide range of Galactic and extragalactic science (see Drlica-Wagner et al. 2021 for examples).

¹ https://delve-survey.github.io

We present the DELVE second data release (DR2), which includes imaging from DELVE, DES, DE-CaLS, and other public DECam programs covering $>21,000 \deg^2$ of sky in g, r, i, and z individually and $\sim 17,000 \, \mathrm{deg}^2$ in all four bands (Figure 1). In comparison to the NOIRLab Source Catalog (Nidever et al. 2018, 2021), the DECam data in DELVE DR2 are processed by the DES Data Management (DESDM; Morganson et al. 2018) pipeline to provide point-spread function (PSF) and automatic aperture measurements for ~ 2.5 billion astronomical sources. In this paper, we describe the DELVE DR2 data set (Section 2) and data reduction pipeline (Section 3). We present studies characterizing the sky coverage, astrometry, photometric calibration, depth, and object classification of the DELVE DR2 catalog in Section 4. In Section 5 we describe how the DELVE DR2 data can be accessed via the NSF's National Optical-Infrared Astronomy Research Laboratory (NOIRLab) Astro Data Lab. Finally, we conclude in Section 6.

2. DATA SET

DELVE DR2 is comprised of 161,380 DECam exposures assembled from > 270 DECam community programs (Appendix A). The largest contributors to the DELVE DR2 data set are DES (DES Collaboration 2021), DECaLS (Dey et al. 2019), DELVE (Drlica-Wagner et al. 2021), and the DECam eROSITA Survey (DeROSITAS: PI Zenteno)². DELVE DR2 more than quadruples the sky area of DELVE DR1 by including exposures in the southern Galactic cap $(b < -10^{\circ})$ and exposures in the northern celestial hemisphere (Dec. > 0°). DELVE DR2 includes data that were collected as part of the DELVE WIDE, MC, and DEEP observing programs (Drlica-Wagner et al. 2021). In addition, DELVE and DeROSITAS have continued to observe regions of the sky that lack DECam imaging to increase the coverage and uniformity of the DECam data set (see Section 3 of Drlica-Wagner et al. 2021). The key properties of the DELVE DR2 data set are listed in Table 1.

Separate criteria were used to select input exposures in the northern Galactic cap, the southern Galactic cap, and the DES region. The northern Galactic cap data set is comprised of DECam exposures with $b>10^{\circ}$ plus an extension into the Galactic plane $(b>0^{\circ})$ in the region of $120^{\circ} < \text{RA} < 140^{\circ}$ to enable an extended analysis of the Jet stellar stream (Jethwa et al. 2018; Ferguson et al.

For each exposure, we calculate the effective depth based on the effective exposure time scale factor, $t_{\rm eff}$, which compares the achieved seeing, sky brightness, and extinction due to clouds relative to canonical values for the site (Neilsen et al. 2016). Exposures in the northern Galactic cap region were required to have an effective exposure time scale factor of $t_{\rm eff} > 0.3$. The requirement on t_{eff} was relaxed in the southern Galactic cap to avoid rejecting exposures taken close to the southern celestial pole. These exposures are observed at high airmass (sec(z) \sim 2) and have systematically worse PSF full width at half maximum (FWHM). Exposures in the southern Galactic cap were required to have $t_{\rm eff} > 0.2$ and $t_{\rm eff} \times T_{\rm exp} > 12 \, \rm s$. No explicit cut was placed on the PSF FWHM in the northern Galactic cap (the cut on t_{eff} removes exposures with very poor seeing), while a cut of FWHM < 1".8 was applied in the southern Galactic cap. The resulting distribution of PSF FWHM and effective exposure time for the full DELVE DR2 data set are shown in Figure 2.

All exposures in the northern and southern Galactic caps were required to have good astrometric solutions when matched to Gaia DR2 (Gaia Collaboration 2018) by SCAMP (Bertin 2006). These criteria required > 250 astrometric matches, $\chi^2_{\rm astrom} < 500$, $\Delta({\rm RA}) < 150\,{\rm mas}$, and $\Delta({\rm Dec}) < 150\,{\rm mas}$. We identified and removed exposures that were heavily contaminated by spurious scattered and reflected light from bright stars using the ray-tracing procedure developed by DES (Kent 2013). In addition, rare failures in the sky background estimation can cause a large number of spurious object detections. A handful of exposures suffering from this processing failure were identified as having a large fraction of unmatched objects, and they were removed from the final catalog production.

DELVE DR2 includes $\sim 60,000$ exposures collected by DES that were processed and calibrated as input into DES DR2 (DES Collaboration 2021).³ The DES processing pipeline required $t_{\rm eff} > 0.2$ for g-band exposures and $t_{\rm eff} > 0.3$ for exposures taken in r, i, and z. DES applied a wavelength-dependent criterion to remove exposures with poor PSF FWHM resulting in a maximum PSF FWHM of $\{1.772, 1.62, 1.56, 1.56\}$ in g, r, i, z, re-

^{2022).} Exposures in the southern Galactic cap were selected to have $b < -10^{\circ}$, excluding exposures within the DES footprint and exposures collected by the DES program. The DES exposures reside in the southern Galactic cap, but they were selected separately when defining the input to DES DR2 (DES Collaboration 2021).

² http://astro.userena.cl/derositas

³ DELVE DR2 does not include the DES Y-band imaging.

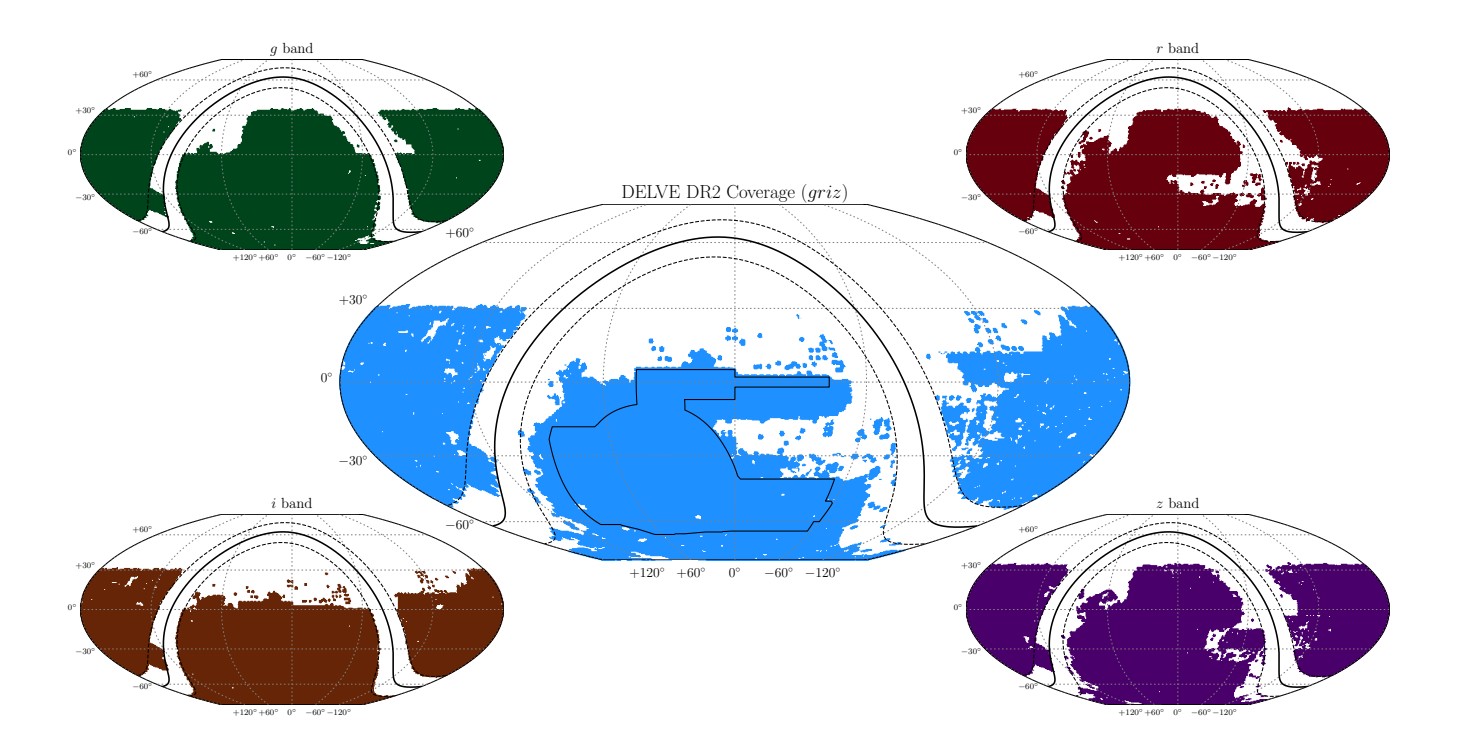


Figure 1. DELVE DR2 covers $> 20,000 \, \text{deg}^2$ in each of the g, r, i, z bands (colored regions) and $\sim 17,000 \, \text{deg}^2$ in all four bands simultaneously (blue region). The $\sim 5,000 \, \text{deg}^2$ footprint of DES is outlined in black. These and other sky maps are shown in the equal-area McBryde–Thomas flat polar quartic projection.

spectively. Additional cuts were applied to remove exposures that were contaminated by stray or scattered light, airplanes, excessive electronic noise, and other artifacts. A full description of the DES data selection and processing criteria can be found elsewhere (Morganson et al. 2018; DES Collaboration 2018, 2021).

3. DATA PROCESSING

All exposures in DELVE DR2 were processed with the DESDM "Final Cut" pipeline (Morganson et al. 2018) as implemented for the processing of DES DR2 (DES Collaboration 2021). Data were reduced and detrended using seasonally averaged bias and flat images, and full-exposure sky background subtraction was performed (Bernstein et al. 2018). SourceExtractor (Bertin & Arnouts 1996) and PSFEX (Bertin 2011) were used to automate source detection and photometric measurement. Astrometric calibration was performed against Gaia DR2 using SCAMP (Bertin 2006). We note that DELVE DR2 does not include the production of coadded images (e.g., DES Collaboration 2018, 2021); how-

ever, we expect that coadded images will be produced as part of a future DELVE data release.

Photometric zeropoints for each DECam CCD were derived independently for the DES exposures and the other DECam exposures included in DELVE DR2. For the DES exposures, we applied zeropoints that were derived for DES DR2 using the forward global calibration module (FGCM; Burke et al. 2018). The FGCM procedure fits time-dependent atmospheric and instrumental conditions to establish an internal network of calibration stars. These calibration stars are then used to iteratively refine the photometric calibration of exposures taken during both photometric and non-photometric The FGCM has been demonstrated to conditions. achieve a relative photometric calibration uncertainty of $\sim 2 \,\mathrm{mmag}$ when applied to the DES exposures (DES Collaboration 2021). In contrast, the non-DES exposures included in DELVE DR2 were calibrated following the simple external calibration procedure developed for DELVE DR1 (Drlica-Wagner et al. 2021). Briefly, we performed a 1" match between objects in the Final Cut catalogs for each DECam CCD and the ATLAS Refcat2 catalog (Tonry et al. 2018). ATLAS Refcat2 covers the entire sky by placing measurements from PS1 DR1 (Chambers et al. 2016), SkyMapper DR1 (Wolf et al. 2018), and several other surveys onto the PS1 q, r, i, z-

⁴ Associated configuration files can be found at: https://github.com/delve-survey/delve_config.

Survey Characteristic		Ва	nd		Reference
	g	r	i	z	
Number of exposures	42034	41852	39003	38491	Section 2
Median PSF FWHM (arcsec)	1.24	1.10	1.02	1.00	Section 2
Sky coverage (individual bands, deg^2)	24663	22939	21283	22866	Section 4.1
Sky coverage $(g, r, i, z \text{ intersection, } \deg^2)$		169	972		Section 4.1
Astrometric repeatability (angular distance, mas)	28	27	28	32	Section 4.2
Astrometric accuracy vs. Gaia (angular distance, mas)		2	2		Section 4.2
Photometric repeatability (mmag)	4.9	5.0	4.5	5.4	Section 4.3
Photometric uniformity vs. Gaia (mmag)	7.2				Section 4.3
Absolute photometric uncertainty (mmag)		≲	20		Section 4.5

24.3

23.9

23.9

23.5

Eff. > 99%; Contam. < 2%

Eff. > 97%; Contam. < 2%

23.5

23.0

22.8

22.4

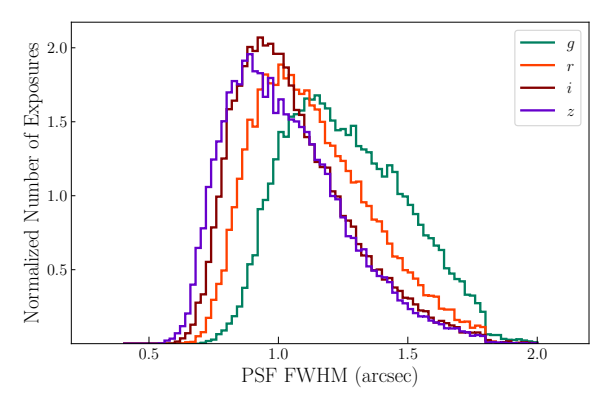
Section 4.6

Section 4.6

Section 4.7

Section 4.7

Table 1. DELVE DR2 key numbers and data quality summary.



Magnitude limit (PSF, S/N = 5)

Magnitude limit (AUTO, S/N = 5)

Galaxy selection (EXTENDED_CLASS $\geq 2,\,19 \leq \texttt{MAG_AUT0_G} \leq 22)$

Stellar selection (EXTENDED_CLASS ≤ 1 , $19 \leq \text{MAG_AUTO_G} \leq 22$)

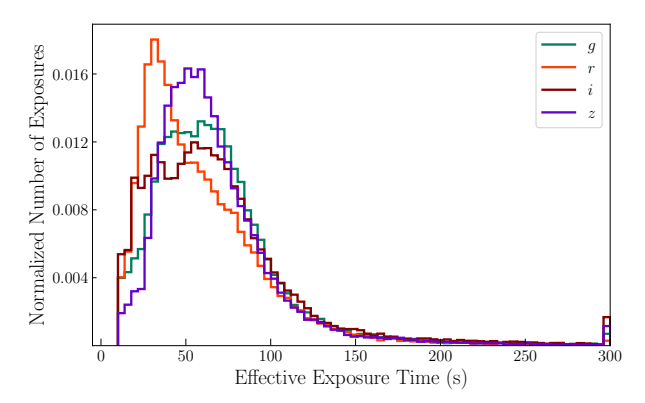


Figure 2. (Left) PSF FWHM distributions for DECam exposures included in DELVE DR2. (Right) Distributions of effective exposure time ($t_{\text{eff}} \times T_{\text{exp}}$) for exposures included in DELVE DR2.

bandpass system. Transformation equations from the ATLAS Refcat2 system to the DECam system were derived by comparing calibrated stars from DES DR1 (Appendix A of Drlica-Wagner et al. 2021). Zeropoints were derived by finding the median offset required to match the DECam observations to the matched ATLAS Refcat2 observations. Zeropoints derived from the DELVE processing and photometric calibration pipeline were found to agree with those derived by DES DR2 with a scatter of $\sim 10\,\mathrm{mmag}$. While the external calibration against ATLAS Refcat2 yields a significantly larger scatter than the FGCM, it can be quickly and easily applied to any DECam exposure.

We built a multi-band catalog of unique sources by combining the SourceExtractor catalogs from each individual CCD image following the procedure described in Drlica-Wagner et al. (2021). We took the

set of SourceExtractor detections with FLAGS < 4, which allowed neighboring and deblended sources, and $(IMAFLAGS_ISO \& 2047) = 0$, which removed objects containing bad pixels within their isophotal radii (Morganson et al. 2018). We further required each detection to have a measured automatic aperture flux, a measured PSF flux, and a PSF magnitude error of < 0.5 mag. We sorted SourceExtractor detections into $\sim 3 \, \mathrm{deg}^2$ (nside = 32) HEALPix pixels (Górski et al. 2005), and within each HEALPix pixel, we grouped detections into clusters by associating all detections within a 0".5 radius. This matching radius was chosen to be significantly larger than the astrometric uncertainty (Section 4.2), but smaller than the PSF FWHM (Figure 2). Furthermore, we identified and split pairs of closely separated objects that were observed in the same image (Drlica-Wagner et al. 2021).

Each cluster of detections was associated with an object in the DELVE DR2 catalog. The astrometric position of each object was calculated as the median of the individual single-epoch measurements of the object. We track two sets of photometric quantities for each object: (1) measurements from the single exposure in each band that has the largest effective exposure time (i.e., the largest $t_{\rm eff} \times T_{\rm exp}$), and (2) the weighted average of the individual single-epoch measurements (these quantities are prefixed by WAVG). The weighted average and unbiased weighted standard deviation were calculated following the weighted sample prescriptions used by DES (Appendix B of DES Collaboration 2021). In addition, we track cluster-level statistics such as the number of detections in each band.

We follow the DES procedure to calculate the interstellar extinction from Milky Way foreground dust (DES Collaboration 2018). We compute the value of E(B-V)at the location of each catalog source by performing a bi-linear interpolation in (RA, Dec) to the maps of Schlegel et al. (1998). The reddening correction for each source in each band, $A_b = R_b \times E(B - V)$, is calculated using the fiducial interstellar extinction coefficients from DES DR1 (DES Collaboration 2018): $R_q = 3.185$, $R_r = 2.140, R_i = 1.571, \text{ and } R_z = 1.196.$ Note that, following the procedure of DES DR1, the Schlafly & Finkbeiner (2011) calibration adjustment to the Schlegel et al. (1998) maps is included in our fiducial reddening coefficients (N = 0.78). The A_b values are included for each object in DELVE DR2, but they are not applied to the magnitude columns by default. The list of the photometric and astrometric properties provided in DELVE DR2 can be found in Appendix B.

3.1. Improvements Relative to DELVE DR1

We have made several improvements to the pipeline described by Drlica-Wagner et al. (2021).

- The seasonally averaged bias and flat images used for image detrending have been updated to include calibration products from the fifth and sixth years of DES observing. The final epoch of DES calibration products have been used to process all exposures taken after the end of DES data taking.
- Images that were heavily affected by reflected or scattered light from bright stars were identified using the DES ray-tracing tool (Kent 2013). Objects detected on these CCDs were removed from the DELVE DR2 catalog.

3. The radius for matching sources within and across bands has been reduced from 1" to 0".5. This change was motivated by the excellent astrometric precision of the DELVE DR1 catalog ($\sim 30\,\mathrm{mas}$). The change, along with improvements in the algorithm for splitting pairs of closely separated objects, reduces the number of objects that are spuriously merged.

4. DATA RELEASE

DELVE DR2 is derived from DECam data covering $> 20,000\,\mathrm{deg}^2$ in each of the g,r,i,z bands, while $\sim 17,000\,\mathrm{deg}^2$ are jointly covered in all four bands (Figure 1). DELVE DR2 consists of a catalog of ~ 2.5 billion unique astronomical objects, with ~ 618 million objects that have measurements in all four bands. This section describes the characterization of the sky coverage, astrometry, photometry, depth, and object classification of the DELVE DR2 catalog. Summary statistics of this characterization are given in Table 1.

4.1. Sky Coverage

We quantify the area covered by DELVE DR2 by pixelizing the geometry of each DECam CCD using the decasu⁶ package built on healsparse.⁷ This package maps the geometry of each CCD using higher-resolution nested HEALPix maps (nside = 16384; $\sim 166 \,\mathrm{arcsec^2}$) and sums the resulting covered pixels to generate lower-resolution maps (nside = 4096; $\sim 0.74 \,\mathrm{arcmin^2}$) containing the fraction of each pixel that is covered by the survey. We quantitatively estimate the covered area as the sum of the coverage fraction maps in each band independently and the intersection of the maps in all four bands (Table 1).

4.2. Astrometry

We assess the internal astrometric repeatability by comparing the distributions of angular separations of individual detections of the same objects over multiple exposures. The median global astrometric spread is 29 mas across all bands and is found to be fairly consistent within each band (Table 1). Furthermore, we estimate the external astrometric accuracy by calculating the angular separation between bright stars in DELVE DR2 (16 < g < 19) and sources in Gaia EDR3 (Gaia Collaboration 2021) matched within 2" (Figure 3). We find that the median separation between the positions measured by DELVE DR2 and Gaia EDR3 is 22 mas, which confirms that no significant astrometric offsets

⁵ Note that we do not apply the "error floor" applied by DES.

⁶ https://github.com/erykoff/decasu

⁷ https://healsparse.readthedocs.io

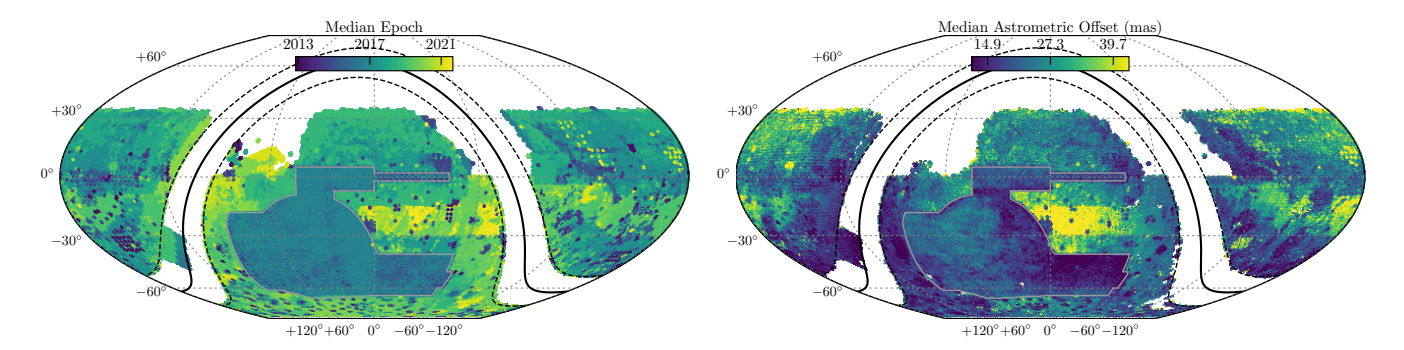


Figure 3. Left: Median observational epoch for DECam observations in all bands (griz) that are used for calculating the coordinates of DELVE DR2 objects. Right: Median astrometric offsets between DELVE DR2 objects with 16 < g < 19 and Gaia EDR3 objects matched within 2". Note that no correction has been made for the proper motions of objects, which results in higher astrometric residuals in regions dominated by recent observations (e.g., see Figure 3 of DES Collaboration 2021).

have been introduced by the catalog coaddition procedure. Since the DESDM astrometric calibration does not incorporate proper motions, we expect some correlation between the astrometric residuals and the median measurement epoch of each source (Figure 3).

4.3. Relative Photometric Calibration

We assess the photometric repeatability in each band from the root-mean-square (rms) scatter between independent PSF magnitude measurements of bright stars. For each band, we select stars with 16 < WAVG_MAG_PSF < 18 mag and calculate the median rms scatter in $\sim 0.2 \, \rm deg^2$ HEALPix pixels (nside = 128). We estimate the median of the rms scatter over the entire footprint in each band. This quantity is found to be $\sim 5 \, \rm mmag$ and is listed for each band in Table 1.

We validate the photometric uniformity of DELVE DR2 by comparing to space-based photometry from Gaia EDR3 (Figure 4). We transform the g, r, i, z photometry from DELVE to the Gaia G band using a set of transformations derived for DES DR2 (Sevilla-Noarbe et al. 2021; DES Collaboration 2021). We compare the Gaia EDR3 G-band magnitude in the AB system (G_{Gaia}) to the predicted G-band magnitude of stars in DELVE (G_{DELVE}). We calculate the median difference, $G_{\text{DELVE}} - G_{Gaia}$, within each nside = 128 HEALPix pixel for stars with $16 < r < 20 \,\mathrm{mag}, \, 0.5 < (g-i) <$ $1.5 \,\mathrm{mag}$, and $Gaia\,G < 20 \,\mathrm{mag}$. We plot the spatial distribution of the median difference along with histograms for the median difference within the DES region and over the full DELVE DR2 footprint in Figure 4. While the median difference within the DES footprint is zero by construction, we find a small (< 1 mmag) offset between DELVE DR2 and Gaia EDR3. We estimate the photometric uniformity of DELVE DR2 as the standard deviation of the median differences across pixels, which yields a value of 7.2 mmag (Table 1). However, because the distribution of residuals is non-Gaussian (Figure 4),

we also provide the 68% containment interval, which is 9.1 mmag. We find no significant magnitude-dependent trends in $G_{\rm DELVE} - G_{Gaia}$ within the magnitude range that we study (16 < r < 20 mag).

Similar comparisons between DES DR2 and Gaia DR2 demonstrated that the nonuniformity of Gaia observations can be the dominant contributor to photometric nonuniformity estimated using this technique (Burke et al. 2018; Sevilla-Noarbe et al. 2021; DES Collaboration 2021). Within the DES footprint, we find that comparing to Gaia EDR3 reveals much less structure than was seen when comparing to Gaia DR2 (DES Collaboration 2021). Furthermore, it is clear that outside the DES footprint, spatial structure in the DELVE DR2 calibration dominates the nonuniformity relative to Gaia. We observe a systematic shift of $\sim 10 \,\mathrm{mmag}$ relative to GaiaEDR3 at Dec = -30° where ATLAS Refcat2 switches from using PS1 to SkyMapper (Tonry et al. 2018; Drlica-Wagner et al. 2021). It should be possible to improve the relative photometric calibration of DELVE by applying the FGCM (Burke et al. 2018). Initial tests using several thousand square degrees of the DELVE data suggest that a relative photometric uniformity of $\lesssim 5 \,\mathrm{mmag}$ is possible.

4.4. Color Uniformity

As an additional check of the color uniformity and relative photometric calibration of DELVE DR2, we perform an analysis of the stellar sequence using the g, r, and i bands (e.g., Ivezić et al. 2004; MacDonald et al. 2004; High et al. 2009; Gilbank et al. 2011; Coupon et al. 2012; Kelly et al. 2014; Drlica-Wagner et al. 2018). The stellar sequence follows a tight locus in the (g-r) vs. (r-i) color-color plane, especially in the region from 0.3 < (g-r) < 1.1. This region of the stellar sequence is dominated by main-sequence stars and has a small intrinsic width. This tight relation allows us to assess the calibration quality in two ways: (1) On small scales, we

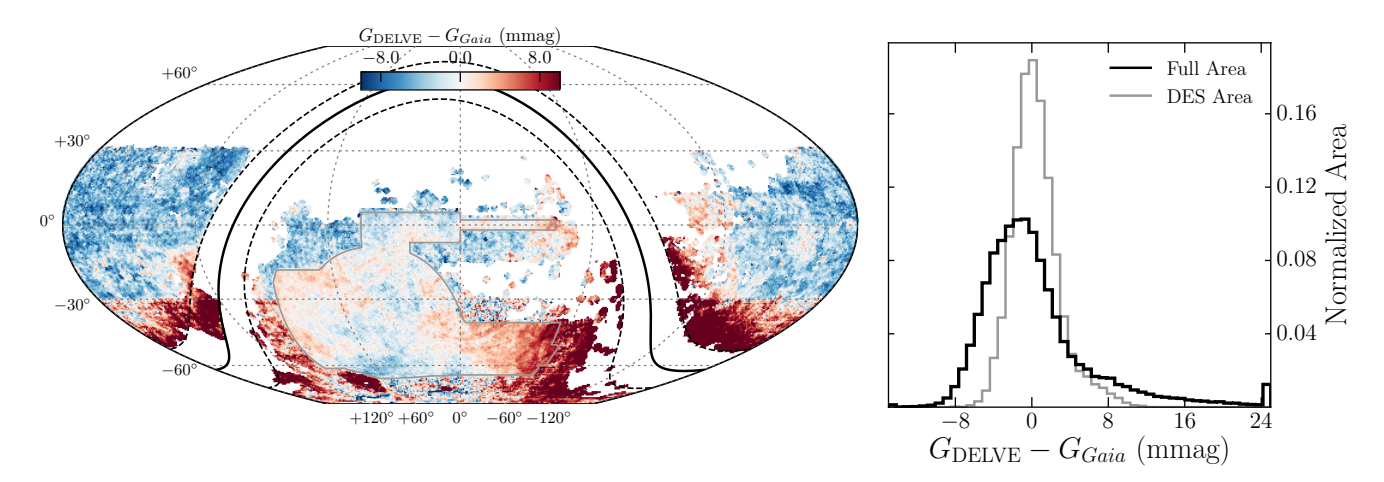


Figure 4. Median difference between the DELVE DR2 photometry transformed into the Gaia G-band, $G_{\rm DELVE}$, and the measured magnitude from Gaia EDR3, $G_{\rm Gaia}$. The spatial distribution of the median difference in each pixel is shown in the left panel (color range clipped to $\pm 10 \,\mathrm{mmag}$), while the right panel shows a histogram of the pixel values. A shift in the zeropoint can be seen at Dec. $\sim -30^{\circ}$, which corresponds to the boundary between the ATLAS Refcat2 use of PS1 and SkyMapper (Section 4.3). This comparison is restricted to the area with overlapping DELVE DR2 coverage in all four bands (g, r, i, z).

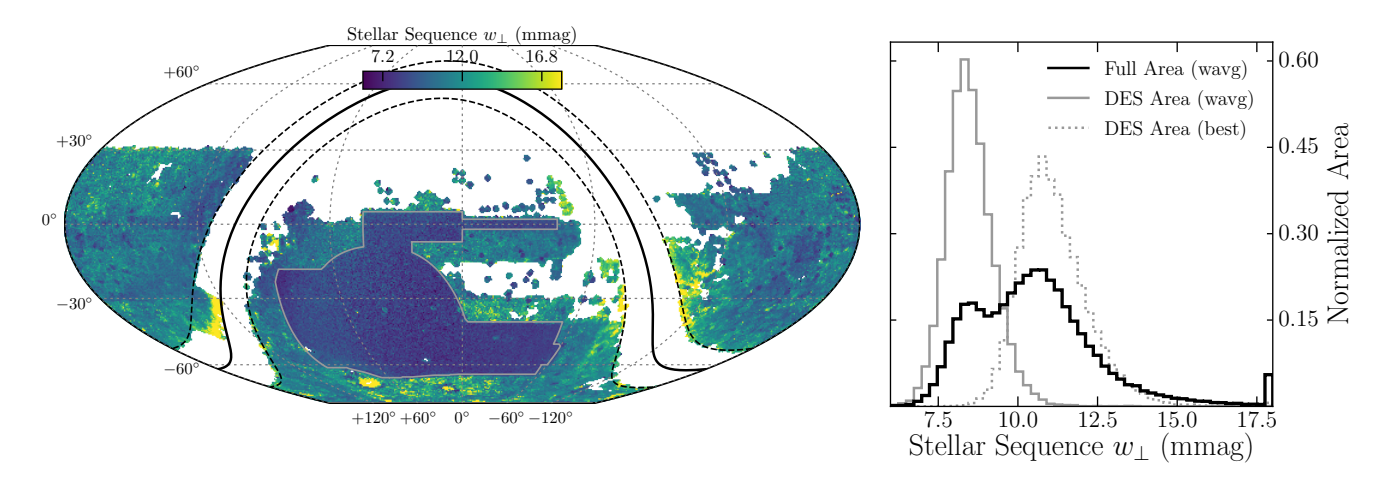


Figure 5. Left: Spatial distribution of the measured width of the stellar locus w_{\perp} using WAVG_MAG_PSF magnitudes for each nside =128 HEALPix pixel in the DELVE DR2 footprint. The DES region can be seen to have much lower values of w_{\perp} indicating a smaller statistical error in these measurements. Right: Histogram of w_{\perp} values ($w_{\perp} = \sqrt{\sigma^2 + w_{\perp,0}^2}$), where $w_{\perp,0} \sim 8$ mmag. The black line shows the same data as the spatial map (WAVG_MAG_PSF magnitudes for the full footprint, a clear bimodality can be seen due to the difference in relative statistical error in measurements between the DES region calibrated with FGCM ($\sigma_{\text{(FGCM, WAVG)}} \sim 3$ mmag), and the rest of the DELVE footprint calibrated with ATLAS Refcat2 ($\sigma_{\text{(ATLAS R2, WAVG)}} \sim 7$ mmag). The gray histograms illustrate the difference in the measured width between the weighted-average (solid) and single best measurements (dotted).

can probe the statistical error in color measurements by computing the width of the stellar sequence (w_{\perp}) . (2) On larger angular scales, we can use variations in the location of this sequence as an estimate of systematic color uniformity.

We follow the method of Ivezić et al. (2004) to measure both the width and location of the stellar sequence. Briefly, we select high-confidence stars (EXTENDED_CLASS_G = 0) that are bright with q, r, and

i extinction-corrected magnitudes brighter than $20 \,\mathrm{mag}$ and extinction-corrected color 0.3 < (g-r) < 1.1.

We performed a linear fit on the data and derived principal components, P_1 and P_2 , where P_2 is perpendicular to the stellar locus line of best fit.

We define w_{\perp} to be the 3σ -clipped rms of the distribution of stars in the P_2 direction. The location of the stellar sequence is summarized as a residual between the (r-i) color of the linear fit at (g-r)=0.7. This value is computed relative to a low extinction (E(B-

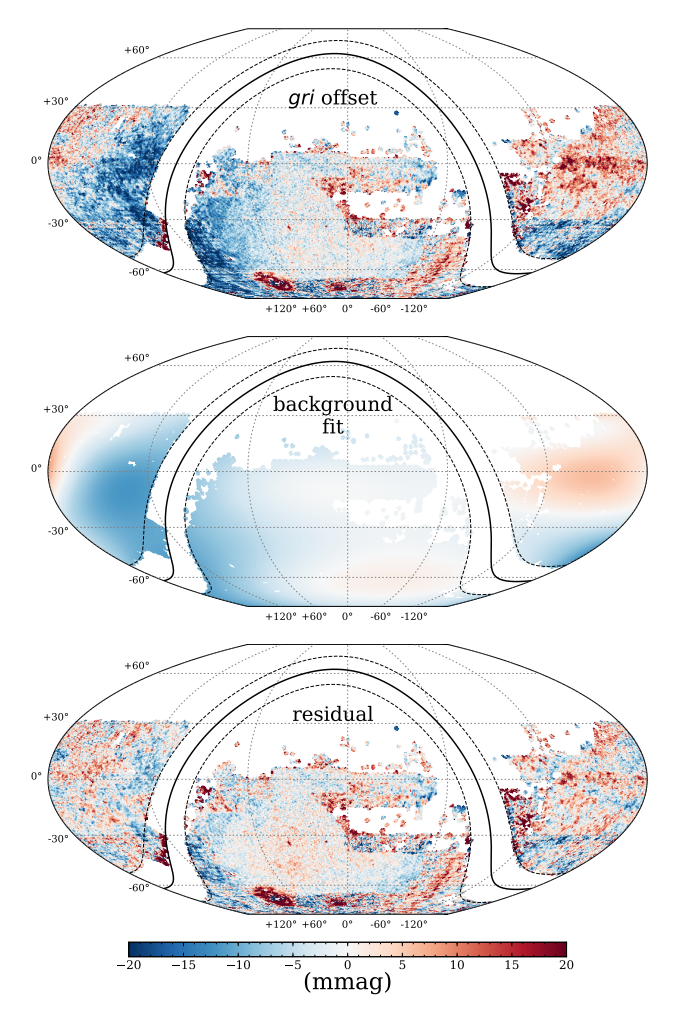


Figure 6. Top: Offset in the stellar locus (r-i) color at (g-r)=0.7 fit in each nside =128 HEALPix pixel relative to the DES value of $(r-i)_{\rm DES}=0.221$ mag. Offsets in this distribution at large spatial scales are likely due to changing stellar populations. Middle: Polynomial fit to the (r-i) offset map smoothed with a $\sigma=5^{\circ}$ Gaussian kernel. Bottom: Map of residuals after the polynomial fit has been subtracted. This residual map highlights variations in the location of the stellar locus at smaller scales and is an estimate of the color uniformity.

V) < 0.015) empirical stellar locus computed from the DES DR2 catalog, where $(r-i)_{\rm DES}=0.221\,{\rm mag}$ at $(g-r)_{\rm DES}=0.7\,{\rm mag}$.

To estimate the magnitude of the statistical error on color, we split our data set into two areas. First, we analyze the DES footprint, which is covered homogeneously and has zeropoints derived from FGCM. Second, we analyze the rest of the DELVE DR2 footprint where zeropoints were derived from ATLAS Refcat2 (Section 3). We calculate the width of the stellar sequence, w_{\perp} , using both the best single-epoch measurement (MAG_PSF) and the weighted-average catalog

measurements (WAVG_MAG_PSF) for each nside = 128 HEALPix pixel. The spatial distribution of w_{\perp} derived from the weighted-average magnitudes can be seen in Figure 5. For the region in the DES footprint, we also compute an estimate of the relative difference in the statistical errors between each type of magnitude measurement, $N_{eff} = \text{MAGERR_PSF}^2/\text{WAVG_MAGERR_PSF}^2$. Assuming that w_{\perp} comes from the statistical uncertainty in the photometric calibration (σ_{stat}) and intrinsic width of the stellar sequence $(w_{\perp,0})$ added in quadrature $(w_{\perp}^2 = \sigma_{\text{stat}}^2 + w_{\perp,0}^2)$, we can use the two measurements of w_{\perp} and effective number of observations (N_{eff}) for the WAVG measurement to solve for σ_{stat} and $w_{\perp,0}$.

Distributions for w_{\perp} in the DES region for the single measurement and \mathtt{WAVG} measurement cases are shown on the right of Figure 5 in gray. We find a median singlemeasurement (WAVG measurement) error of $\sigma_{\rm (FGCM)} \sim 8$ mmag ($\sigma_{(FGCM, WAVG)} \sim 3$ mmag) for the region with zeropoints derived from FGCM and a median intrinsic width of the stellar locus $w_{\perp,0} \sim 8$ mmag. To estimate $\sigma_{\rm stat}$ for the ATLAS Refcat2 calibrated region where the coverage is not as homogeneous, we use the $w_{\perp,0}$ estimate from the FGCM region. The median single-measurement (WAVG measurement) error of $\sigma_{(\text{ATLAS R2})} \sim 10 \text{ mmag} \left(\sigma_{(\text{ATLAS R2, WAVG})} \sim 7 \text{ mmag}\right)$ for the region with zeropoints derived from ATLAS Refcat2. This value of $\sigma_{(ATLAS\,R2,\,WAVG)}$ agrees with the comparison to Gaia EDR3 data in Section 4.3. Furthermore, this analysis highlights the differences in color uncertainty between the FGCM calibrated region and the ATLAS Refcat2 calibrated region. We note that variations in reddening and underlying stellar populations could cause variations in the intrinsic width of the stellar locus, and our value in the DES region of $w_{\perp,0}=8$ mmag can be thought of as a lower limit over the rest of the sky. Therefore, the inferred $\sigma_{(ATLAS\,R2)}$ is an upper limit on the statistical color uncertainty in the ATLAS Refcat2 calibrated region.

As described above, we use the position of the stellar locus in the (g-r) vs. (r-i) plane as a probe of color uniformity in DELVE. Similar to w_{\perp} , we use the results of our fit calculated for each nside = 128 HEALPix pixel. The offsets between the calculated value and the DES Y6 value for each HEALPix pixel are shown in the top panel of Figure 6. Using MAG_PSF (WAVG_MAG_PSF), we find a median rms in the (r-i) color of the linear fit at (g-r)=0.7 of 9 mmag (8 mmag) for the entire survey footprint, with a scatter between MAG_PSF and WAVG_MAG_PSF of less than 3 mmag. If we compare the DES footprint to the rest of the DELVE using MAG_PSF, we find median rms measurements of 5 mmag and 9 mmag, respectively. It is likely that some of this scatter

can be attributed to the effects of interstellar extinction and changes in the observed stellar populations across the footprint, which will shift the location of the stellar locus (see Section 2.3 of High et al. 2009). To estimate the effect of reddening on these values, we compute a median rms only for regions with $E(B-V) < 0.5 \,\mathrm{mag}$ and find that our results are unchanged. This indicates that reddening systematics do not strongly contribute to the spatial structure seen in the top row of Figure 6. In order to account for shifts of the stellar locus on large spatial scales (tens of degrees) and estimate the color uniformity on scales of a few degrees, we smooth the spatial distribution of the residuals with a Gaussian kernel with a standard deviation of $\sigma = 5^{\circ}$ and fit a fifth-order polynomial. This polynomial is then subtracted from the spatial distribution, mitigating the effect of spatially dependent changes in the location of the stellar locus and highlighting systematic scatter in the color uniformity at scales of a few degrees. Using this subtracted map, we find a median rms of 4 mmag for the DES region and 7 mmag for the rest of the DELVE DR2 footprint. This can be interpreted as a lower limit on the systematic uncertainties in the color measurements of DELVE DR2.

4.5. Absolute Photometric Calibration

The photometry of DELVE DR2 is tied to the ABmagnitude system (Oke & Gunn 1983) via the HST CalSpec standard star C26202. Within the DES footprint, the DES FGCM zeropoints are directly tied to C26202, as described in Section 4.2.2 of DES Collaboration (2021). Outside the DES footprint, the calibration is tied more indirectly to C26202 via the zeropoints of the ATLAS Refcat2 transformation equations, which were adjusted to match DES DR2 (see Appendix A of Drlica-Wagner et al. 2021). Due to this procedure, DELVE DR2 cannot have a better absolute calibration accuracy than DES DR2, which sets a lower limit on the statistical uncertainty of 2.2 mmag per band and a systematic uncertainty of 11 to 12 mmag per band (see Table 1 of DES Collaboration 2021). The global offset seen between the PS1 and SkyMapper regions of ATLAS Refcat2 when compared to Gaia EDR3 suggests that the absolute calibration cannot be better than 10 mmag. Combining the maximum systematic uncertainty on the absolute calibration from DES DR2 and the DELVE DR2 offset relative to Gaia EDR3, we estimate that the absolute photometric accuracy of DELVE DR2 is $\lesssim 20 \,\mathrm{mmag}$.

DELVE performed dedicated observations of the Cal-Spec standard star SDSS151421 during twilight hours in 2020. These observations were not used to set the abso-

Table 2. DELVE DR2 median depth estimates.

Measurement	Magnitude Limit					
	$g \pmod{mag}$	$r \pmod{mag}$	$i \pmod{mag}$	$z \pmod{mag}$		
MAG_PSF (S/N=5)	24.3	23.9	23.5	22.8		
$MAG_PSF (S/N=10)$	23.5	23.1	22.7	22.1		
$\mathtt{MAG_AUTO}~(\mathrm{S/N}{=}5)$	23.9	23.5	23.0	22.4		
MAG_AUTO $(S/N=10)$	22.8	22.5	22.1	21.4		

NOTE—The MAG_PSF depth is estimated from point-like sources, while the MAG_AUTO depth is estimated from all DELVE DR2 sources. Both MAG_PSF and MAG_AUTO are estimated from the best exposure of each object (see Section 4.6).

lute calibration of DELVE DR2, and they can instead be used to validate our estimate of the absolute calibration uncertainty. We find that the median offsets between the DELVE PSF magnitudes and the CalSpec STIS magnitudes for SDSS151421 are Δg =4.4, Δr =23.3, Δi =7.2, and Δz =1.6 mmag with a scatter of \sim 6 mmag. Similar analyses performed by DES found \sim 10 mmag offsets when comparing the DES photometry to several CalSpec standard stars and DA white dwarfs within the DES footprint (DES Collaboration 2021). Based on these comparisons, we maintain the stated absolute calibration accuracy of \lesssim 20 mmag.

4.6. Photometric Depth

The photometric depth of DELVE DR2 can be assessed in several ways. One common metric is to determine the magnitude at which a fixed signal-to-noise ratio (S/N) is achieved (e.g., Rykoff et al. 2015). The statistical magnitude uncertainty is related to the S/N calculated from the flux, $F/\delta F$, via propagation of uncertainties and Pogson's law (Pogson 1856),

$$\delta m = \frac{2.5}{\ln 10} \frac{\delta F}{F}.\tag{1}$$

Using this equation, we estimate the magnitude at which DELVE DR2 achieves S/N=5 ($\delta m \approx 0.2171$) and S/N=10 ($\delta m \approx 0.1085$). We calculate these magnitude limits for point-like sources using MAG_AUTO. For each magnitude and S/N combination, we select objects and interpolate the relation between m and median(δm) in $\sim 12\,\mathrm{arcmin^2}$ HEALPix pixels (nside = 1024). The resulting median magnitude limits estimated over the DELVE DR2 footprint are shown in Table 2. We show histograms of the MAG_PSF magnitude limit for point-like sources at S/N=5

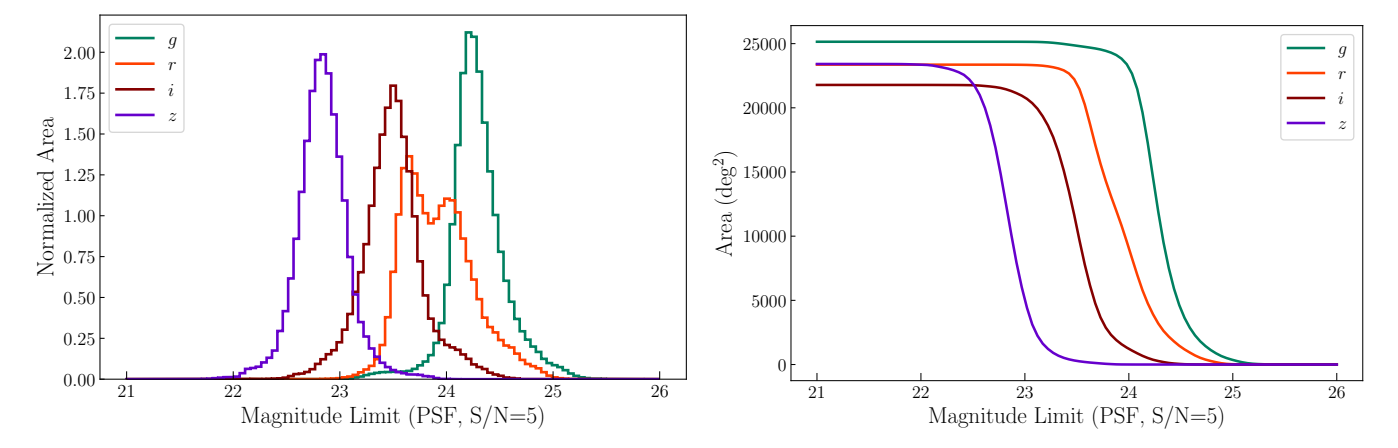


Figure 7. (Left) Distribution of PSF magnitude limits for point-like sources at S/N=5. The double-peaked structure in r band comes from the different exposure times used in DES and DECaLS. (Right) DELVE DR2 survey area in each band as a function of the limiting PSF magnitude (S/N=5). These distributions look similar when calculated from the MAG_AUTO limiting magnitude for all sources, but are shifted brighter by ~ 0.4 mag.

in the left panel of Figure 7. In the right panel of Figure 7 we show the DELVE DR2 area as a function of depth in each band. The magnitude limits as a function of location on the sky are shown in Appendix C. Due to the catalog-level coaddition process, the depth of DELVE DR2 is set by the single best exposure in any region of the sky. This means that the depth of DELVE DR2 is very similar to that of DELVE DR1 (Drlica-Wagner et al. 2021) and significantly shallower than DES DR2 even in the overlapping DES region (DES Collaboration 2021). At bright magnitudes, the DE-Cam CCDs will saturate at q = 15.2, r = 15.7, i = 15.8, and z = 15.5 for point sources observed in a 90 s exposure with median seeing (DES Collaboration 2021). While $\sim 85\%$ of the exposures included in DELVE DR2 have exposure times of $\lesssim 90\,\mathrm{s}$, there are some regions with longer exposure times where saturation will occur at fainter magnitudes. Therefore, objects detected by SourceExtractor with the saturation flag bit set were removed from the DELVE DR2 catalog production.

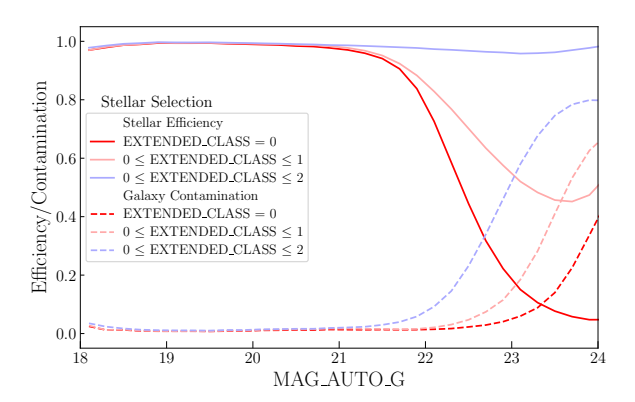
4.7. Object Classification

DELVE DR2 includes the SourceExtractor SPREAD_MODEL parameter, which can be used to separate spatially extended galaxies from point-like stars and quasars (e.g., Desai et al. 2012). Following DES (e.g., DES Collaboration 2018, 2021) and DELVE DR1 (Drlica-Wagner et al. 2021), we define EXTENDED_CLASS parameters as a sum of several Boolean conditions,

```
\begin{split} & \texttt{EXTENDED\_CLASS\_G} = \\ & \quad \left( (\texttt{SPREAD\_MODEL\_G} + 3 \, \texttt{SPREADERR\_MODEL\_G}) > 0.005) \\ & \quad + ((\texttt{SPREAD\_MODEL\_G} + \texttt{SPREADERR\_MODEL\_G}) > 0.003) \\ & \quad + ((\texttt{SPREAD\_MODEL\_G} - \texttt{SPREADERR\_MODEL\_G}) > 0.003). \end{split}
```

When true, each Boolean condition adds one unit to the classifier such that an EXTENDED_CLASS value of 0 indicates high-confidence stars, 1 is likely stars, 2 is likely galaxies, and 3 is high-confidence galaxies. Objects that lack coverage in a specific band or where the SPREAD_MODEL fit failed are set to a sentinel value of -9. We calculate EXTENDED_CLASS values similarly for each band; however, we recommend the use of the g-band classifier, EXTENDED_CLASS_G, because the g band has the widest coverage and deepest limiting magnitude.

In Figure 8, we characterize the performance of EXTENDED_CLASS_G as a function of magnitude by matching DELVE DR2 objects to data from the Spring equatorial field (128° \lesssim RA \lesssim 225°; $-2^{\circ} \lesssim$ Dec \lesssim 5°) of the Wide layer of Hyper Suprime-Cam Subaru Strategic Program Public Data Release 3 (HSC-SSP PDR3 Aihara et al. 2022). To improve uniformity, we select only overlapping regions where the S/N = 5 limiting PSF magnitude from DELVE is representative of the DELVE DR2 survey (magnitude limit of 24 < q < 24.5; Appendix C). The superior image quality (*i*-band PSF FWHM ~ 0.61) and depth ($i \sim 26.2 \,\mathrm{mag}$) of the Wide layer of HSC-SSP PDR3 enable robust tests of stargalaxy separation in DELVE DR2. The matched data set covers $\sim 394 \, \mathrm{deg}^2$ and contains ~ 9.6 million matched objects. Following previous analyses (DES Collaboration 2018; Drlica-Wagner et al. 2021), we select pointlike sources from HSC-SSP PDR3 based on the difference between the i-band PSF and model magnitudes of sources,



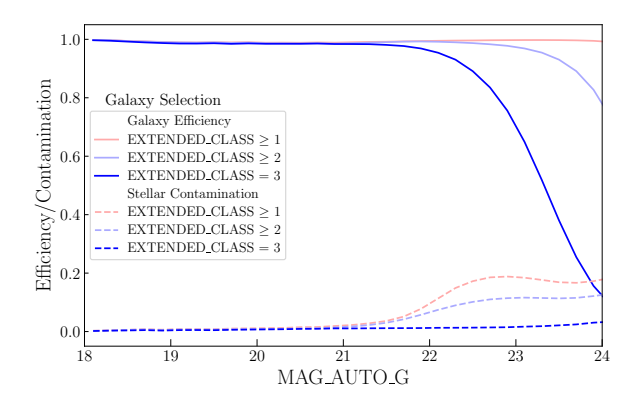


Figure 8. DELVE DR2 star/galaxy classification performance as a function of magnitude estimated from matched objects in the wide layer of HSC-SSP PDR3. *Left:* Stellar efficiency and galaxy contamination for several stellar samples based on EXTENDED_CLASS_G. *Right:* Galaxy efficiency and stellar contamination as a function of magnitude for several galaxy samples based on EXTENDED_CLASS_G.

This scheme requires that the PSF and model magnitudes are very similar for fainter sources, while the agreement is relaxed for brighter sources. This selection results in $\sim\!7.1$ million matched objects classified as galaxies and $\sim\!2.5$ million matched objects classified as stars. We use these objects to evaluate the differential performance of DELVE DR2 EXTENDED_CLASS_G as a function of magnitude in Figure 8. A nominal stellar sample (0 \leq EXTENDED_CLASS_G \leq 1) contains $\sim\!621$ million objects, while a nominal galaxy sample (2 \leq EXTENDED_CLASS_G) contains $\sim\!749$ million objects. We report the integrated efficiency and contamination of these samples over the magnitude range $19 \leq$ MAG_AUTO_G \leq 22 mag in Table 1.

The spatial number density of high-confidence stars (EXTENDED_CLASS_G = 0) and high-confidence galaxies (EXTENDED_CLASS_G = 3) are shown in Figure 9. The stellar density map clearly shows increasing stellar density toward the Galactic plane, as well as the high stellar density associated with the Large Magellanic Cloud (LMC) and Small Magellanic Cloud (SMC). The galaxy density map is dominated by the large-scale clustering of galaxies at high Galactic latitudes, but stellar contamination is apparent close to the Galactic bulge, LMC, and SMC. These maps have had a magnitude cut applied at MAG_AUTO_I < 22 and have not been corrected for interstellar extinction, so some apparent variations in depth come from the extinction, while others come from actual variations in depth over the footprint.

4.8. Known Issues

1. The DESDM pipeline was designed for galaxy photometry at high Galactic latitudes. Sky subtraction and deblending suffer in regions of high stellar density. This leads to degraded photometry and object classification in these regions, most no-

- tably close to the Galactic plane and the Magellanic Clouds (Figure 9).
- The star-galaxy classification efficiency varies over the footprint in a way that is found to correlate with imaging depth and object density. Care should be taken in regions of high density and/or spatially variable depth.
- 3. While the impact of scattered light from bright stars and failures in the sky background estimation have been mitigated in DELVE DR2 (Section 2), some localized, low-level catalog contamination does remain. The effects of scattered light may be further mitigated through the use of more advanced identification algorithms (e.g., Tanoglidis et al. 2022).
- 4. Spatial coverage maps were created at a resolution of $\mathtt{nside} = 16384$, corresponding to linear pixel dimensions of $\sim 13''$. Thus, there are a small number of catalog objects that reside outside the coverage maps due to the slight inaccuracy at the CCD boundaries. These objects reside at the edges of the DELVE footprint and are < 0.0001% of the catalog.

5. DATA ACCESS

Access to DELVE DR2 is provided through the Astro Data Lab (Fitzpatrick et al. 2016; Nikutta et al. 2020), part of the Community Science and Data Center (CSDC) hosted by NOIRLab. DELVE DR2 includes a main object table consisting of photometric measurements for ~ 2.5 billion objects. In addition, the Astro Data Lab has computed cross-match tables be-

⁸ https://datalab.noirlab.edu

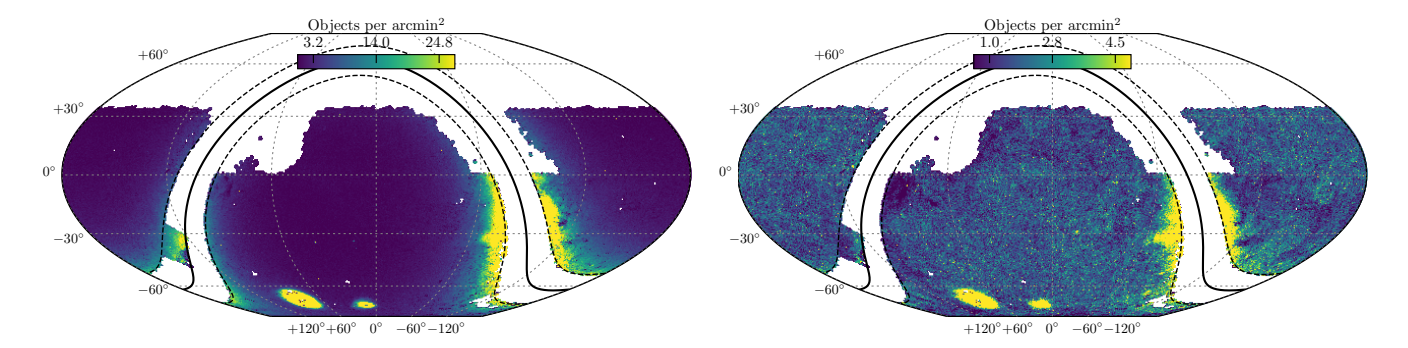


Figure 9. Left: Stellar density map created with the EXTENDED_CLASS_G = 0 (high-confidence stars) selection described in Section 4.7. Right: Analogous galaxy counts map created with the EXTENDED_CLASS_G = 3 (high-confidence galaxies) selection. The region of lower galaxy density toward the northeast of the footprint can be attributed to higher interstellar extinction, which is not corrected for in this map. Color range units are number of objects per arcmin². Both maps apply a magnitude threshold of MAG_AUTO_G < 22.

tween the DELVE DR2 catalog and catalogs from All-WISE, Gaia EDR3, NSC DR2, SDSS DR16, and un-WISE DR1 (Cutri et al. 2021; Gaia Collaboration 2021; Nidever et al. 2021; Ahumada et al. 2020; Schlafly et al. 2019). These cross-match tables and their reverse counterparts are served alongside the DELVE DR2 main object table at the Astro Data Lab (see Appendix B). The DELVE DR2 catalog data can be accessed via both a Table Access Protocol (TAP)⁹ service and from direct PostgreSQL queries via web-based, command-line, and programmatic query interfaces. In addition, the Astro Data Lab provides an image cutout service, built on the Simple Image Access (SIA) protocol, that can be used to access versions of the DELVE DR2 imaging data processed with the DECam Community Pipeline (Valdes et al. 2014). More detailed information on accessing the DELVE DR2 data can be found on the Astro Data Lab website. 10

6. SUMMARY

DELVE seeks to study the physics of dark matter and galaxy formation by observing resolved dwarf galaxies and stellar substructures in the Local Volume. To do so, DELVE has set out to complete contiguous deep imaging coverage of the southern high Galactic latitude sky. DELVE DR2 combines new observations with archival DECam data to cover $> 20,000 \, \text{deg}^2$ individually in g, r, i, z and $\sim 17,000 \, \text{deg}^2$ in all four bands simultaneously. The DELVE DR2 catalog contains PSF and automatic aperture measurements for ~ 2.5 billion astronomical objects with a 5σ PSF depth of $g = 24.3, r = 23.9, i = 23.5, z = 22.8 \, \text{mag}$ (Table 1).

The DELVE DR2 data products are accessible through the NOIRLab Astro Data Lab.

As of 2022 January, DELVE has completed $\sim 80\%$ of its 126 nights of scheduled DECam observing. Additional DECam observations will increase the coverage, uniformity, and depth of future DELVE catalogs. Furthermore, we expect that future DELVE data releases will include products derived from image coaddition, as well as deeper targeted regions of the DELVE footprint. We anticipate that DELVE DR2 and future DELVE data releases will be a valuable resource for the community in advance of the Vera C. Rubin Observatory Legacy Survey of Space and Time.

7. ACKNOWLEDGMENTS

The DELVE project is partially supported by Fermilab LDRD project L2019-011, the NASA Fermi Guest Investigator Program Cycle 9 grant 91201, and the National Science Foundation (NSF) under grant AST-2108168. This work is supported by the Fermilab Visiting Scholars Award Program from the Universities Research Association.

ABP acknowledges support from NSF grant AST-1813881. JLC acknowledges support from NSF grant AST-1816196. JDS acknowledges support from NSF grant AST-1714873. SRM acknowledges support from NSF grant AST-1909497. DJS acknowledges support from NSF grants AST-1821967 and AST-1813708. DC acknowledges support from NSF grant AST-1814208. BMP acknowledges support from the NSF Astronomy and Astrophysics Postdoctoral Fellowship under award AST-2001663. SM acknowledges support from the NSF Graduate Research Fellowship under grant DGE-1656518. DMD acknowledges financial support from the State Agency for Research of the Spanish MCIU through the "Centre of Excellence Severo Ochoa" award for the Instituto de Astrofísica de Andalucía (SEV-2017-

⁹ http://ivoa.net/documents/TAP

¹⁰ https://datalab.noirlab.edu/delve

0709). CPMB and MRLC acknowledge support from the European Research Council (ERC) under the European Union's Horizon 2020 research and innovation programme (grant agreement no. 682115). LSS acknowledges the financial support from FAPESP through the grant #2020/03301-5. JACB acknowledges support from ANID FONDECYT Regular 1220083.

Funding for the DES Projects has been provided by the U.S. Department of Energy, the U.S. National Science Foundation, the Ministry of Science and Education of Spain, the Science and Technology Facilities Council of the United Kingdom, the Higher Education Funding Council for England, the National Center for Supercomputing Applications at the University of Illinois at Urbana-Champaign, the Kavli Institute of Cosmological Physics at the University of Chicago, the Center for Cosmology and Astro-Particle Physics at the Ohio State University, the Mitchell Institute for Fundamental Physics and Astronomy at Texas A&M University, Financiadora de Estudos e Projetos, Fundação Carlos Chagas Filho de Amparo à Pesquisa do Estado do Rio de Janeiro, Conselho Nacional de Desenvolvimento Científico e Tecnológico and the Ministério da Ciência, Tecnologia e Inovação, the Deutsche Forschungsgemeinschaft and the Collaborating Institutions in the Dark Energy Survey.

The Collaborating Institutions are Argonne National Laboratory, the University of California at Santa Cruz, the University of Cambridge, Centro de Investigaciones Energéticas, Medioambientales y Tecnológicas-Madrid, the University of Chicago, University College London, the DES-Brazil Consortium, the University of Edinburgh, the Eidgenössische Technische Hochschule (ETH) Zürich, Fermi National Accelerator Laboratory, the University of Illinois at Urbana-Champaign, the Institut de Ciències de l'Espai (IEEC/CSIC), the Institut de Física d'Altes Energies, Lawrence Berkeley National Laboratory, the Ludwig-Maximilians Universität München and the associated Excellence Cluster Universe, the University of Michigan, NSF's NOIRLab, the University of Nottingham, The Ohio State University, the University of Pennsylvania, the University of Portsmouth, SLAC National Accelerator Laboratory, Stanford University, the University of Sussex, Texas A&M University, and the OzDES Membership Consortium.

The DES data management system is supported by the National Science Foundation under Grant Numbers AST-1138766 and AST-1536171. The DES participants from Spanish institutions are partially supported by MICINN under grants ESP2017-89838, PGC2018-094773, PGC2018-102021, SEV-2016-0588, SEV-2016-

0597, and MDM-2015-0509, some of which include ERDF funds from the European Union. IFAE is partially funded by the CERCA program of the Generalitat de Catalunya. Research leading to these results has received funding from the European Research Council under the European Union's Seventh Framework Program (FP7/2007-2013) including ERC grant agreements 240672, 291329, and 306478. We acknowledge support from the Brazilian Instituto Nacional de Ciência e Tecnologia (INCT) do e-Universo (CNPq grant 465376/2014-2).

Based in part on observations at Cerro Tololo Inter-American Observatory at NSF's NOIRLab, which is managed by the Association of Universities for Research in Astronomy (AURA) under a cooperative agreement with the National Science Foundation.

This work has made use of data from the European Space Agency (ESA) mission *Gaia* (https://www.cosmos.esa.int/gaia), processed by the *Gaia* Data Processing and Analysis Consortium (DPAC, https://www.cosmos.esa.int/web/gaia/dpac/consortium). Funding for the DPAC has been provided by national institutions, in particular the institutions participating in the *Gaia* Multilateral Agreement.

This paper is based on data collected at the Subaru Telescope and retrieved from the HSC data archive system, which is operated by the Subaru Telescope and Astronomy Data Center (ADC) at NAOJ. Data analysis was in part carried out with the cooperation of Center for Computational Astrophysics (CfCA), NAOJ. We are honored and grateful for the opportunity of observing the Universe from Maunakea, which has the cultural, historical and natural significance in Hawaii.

This manuscript has been authored by Fermi Research Alliance, LLC under Contract No. DE-AC02-07CH11359 with the U.S. Department of Energy, Office of Science, Office of High Energy Physics.

Facilities: Blanco (DECam), Astro Data Lab, Gaia, Subaru (HSC)

Software: astropy (Astropy Collaboration 2018), fitsio, ¹¹ HEALPix (Górski et al. 2005), ¹² healpy (Zonca et al. 2019), ¹³ healsparse, ¹⁴ matplotlib (Hunter 2007), numpy (Harris et al. 2020), PSFEx (Bertin 2011),

¹¹ https://github.com/esheldon/fitsio

¹² http://healpix.sourceforge.net

¹³ https://github.com/healpy/healpy

¹⁴ https://healsparse.readthedocs.io/en/latest/

scipy (Virtanen et al. 2020), SCAMP (Bertin 2006), skymap, 15 SourceExtractor (Bertin & Arnouts 1996)

APPENDIX

 $^{^{15}\;\}rm https://github.com/kadrlica/skymap$

A. DECAM DATA

DELVE DR2 combines DECam observations acquired by 278 programs. These programs and the number of exposures they each contributed to DELVE DR2 are listed in Table 3.

Table 3. DECam data included in DELVE DR2

Prop.ID	PI	$N_{ m exp}$	Prop.ID	PI	$N_{ m exp}$	Prop.ID	PI	$N_{ m exp}$
2012B-0001	Josh Frieman	63656	2018A-0909	Thomas H Puzia	121	2012B-0620	Jeremy Mould	23
2014B-0404	David Schlegel	28823	2015A-0631	Alfredo Zenteno	120	2021A-0010	Travis Rector	23
2019A-0305	Alex Drlica-Wagner	12459	2017B-0312	Bryan Miller	119	2019B-0080	Casey Papovich	23
2018A-0386	Alfredo Zenteno	3029	2019A-0265	Douglas P Finkbeiner	119	2013A-0737	Scott Sheppard	22
2013B-0440	David Nidever	2753	2016B-0124	Edo Berger	111	2016A-0622	Paulo Lopes	22
2019A-0272	Alfredo Zenteno	2452	2013B-0421	Armin Rest	107	2016A-0191	Armin Rest	22
2017A-0260	Marcelle Soares-Santos	2297	2020A-0058	Kathy Vivas	107	2012B-3001	Emmanuel Bertin	21
2021A-0149	Alfredo Zenteno	1886	2015B-0606	Katharine Lutz	106	2015A-0322	R Michael Rich	21
2016A-0366	Keith Bechtol	1870	2020A-0402		102	2019A-0240		20
2019B-0323	Alfredo Zenteno	1586	2015B-0187	Edo Berger	98	2018A-0371	Sangeeta Malhotra	20
2017A-0388	Alfredo Zenteno	1432	2017B-0906	Dougal Mackey	97	2012B-0625	Sarah Sweet	20
2018A-0242	Keith Bechtol	1423	2017A-0298	Brad Tucker	96	2014A-0496	Aren Heinze	20
2020A-0399	Alfredo Zenteno	1387	2018A-0159	Kathy Vivas	96	2019B-0256	Michael M Shara	20
2021A-0275	Armin Rest	1336	2014A-0339	Jonathan Hargis	95	2012B-0621	Loren Bruns	19
2018A-0273	William Dawson	1192	2014A-0622	Iraklis Konstantopoulos	92	2012B-0021 2014B-0265	Ian Dell'Antonio	19
2018A-0213 2018A-0913	Brad Tucker	1086	2014A-0022 2020A-0910	Thomas H Puzia	91	2014B-0203 2015B-0175	Anton Koekemoer	19
	David Schlegel	997		Armin Rest	90		Gastao B Lima Neto	18
2013A-0741			2018A-0380			2013B-0627 2014A-0621		
2019A-0308	Ian Dell'Antonio	944	2019B-0403	Clara Martinez-Vazquez	87		Dougal Mackey	18
2013A-0327	Armin Rest	900	2014A-0239	Mark Sullivan	83	2013A-9999	Alistair Walker	18
2014A-0624	Helmut Jerjen	817	2018B-0941	Alistair Walker	82	2014A-0634	David James	17
2017B-0279	Armin Rest	790	2018A-0137	Jeffrey Cooke	76	2014B-0611	Douglas P Geisler	17
2013A-0214	Maureen Van Den Berg	772	2014A-0429	Douglas P Finkbeiner	74	2013A-0386	Paul Thorman	16
2013A-0360	Anja von der Linden	737	2017B-0239	Keith Bechtol	72	2014A-0073	Mukremin Kilic	16
2013A-0724	Lori Allen	708	2013B-0612	Julio Chaname	71	2015A-0618	Chris Lidman	15
2018A-0914	Martin Makler	704	2019A-0065	Yue Shen	70	2014B-0375	Armin Rest	15
2015A-0608	Francisco Forster	638	2018B-0340	Herve Bouy	70	2014A-0386	Ian Dell'Antonio	15
2014A-0415	Anja von der Linden	604	2015A-0151	Annalisa Calamida	70	2014B-0610	Julio Chaname	14
2014A-0306	Xinyu Dai	559	2014A-0348	Haojing Yan	68	2012B-3005	Knut Olsen	14
2015A-0616	Helmut Jerjen	467	2017B-0285	Armin Rest	68	2019A-0337	David E Trilling	14
2016B-0909	Camila Navarrete	462	2017B-0078	Herve Bouy	68	2014B-0064	Mukremin Kilic	14
2013A-0614	Sarah Sweet	460	2019A-0235		67	2016A-0337	Genaro Suarez Castro	12
2016B-0301	Armin Rest	439	2018B-0905	Stree Oh	66	2017A-0951	Kathy Vivas	12
2019B-1014	Felipe Olivares	437	2014A-0632	Tiago Gonçalves	65	2013A-0351	Arjun Dey	12
2015A-0620	Ana Bonaca	430	2020A-0353	Eric Peng	65	2013B-0615	Julio Carballo-Bello	12
2014A-0035	Herve Bouy	427	2016A-0384	Jacqueline McCleary	64	2015A-0062	Linda French	12
2018B-0271	Douglas P Finkbeiner	424	2014A-0480	R Michael Rich	63	2019B-1013	Thomas H Puzia	12
2019A-0910	Dougal Mackey	424	2014A-0313	Kathy Vivas	62	2015A-0610	Cesar Fuentes	12
2015A-0110	Thomas De Boer	379	2015B-0307	Armin Rest	61	2014B-0613	Jeffrey Cooke	11
2014A-0270	Carl J Grillmair	363	2018A-0206	Abhijit Saha	61	2014B-0614	Iraklis Konstantopoulos	11
2016A-0189	Armin Rest	359	2015A-0617	David M Nataf	60	2012B-0623	Dougal Mackey	10
2013A-0411	David Nidever	358	2017A-0210	Alistair Walker	60	2016A-0095	Jeffrey Cooke	10
2016A-0618	Dougal Mackey	349	2013B-0617	Dougal Mackey	59	2016A-0951		10
2020A-0018	Felipe Olivares	339	2013A-0529	R Michael Rich	59	2015A-0175	Taran Esplin	9
2014A-0608	Francisco Forster	335	2014B-0193	Frederick M Walter	58	2013B-0453	Scott Sheppard	9
2014A-0008 2016A-0190	Arjun Dey	333	2014B-0193 2017B-0103	Wayne Barkhouse	58	2013B-0433 2018B-0327	Sangeeta Malhotra	9
2010A-0190 2021A-0922	Jose L Nilo Castellon	332	2017B-0103 2019B-0042	Herve Bouy	56 57	2018B-0327 2015A-0609	Julio Carballo-Bello	9
2021A-0922 2020B-0241				· ·				
2020B-0241 2018A-0251	Alfredo Zenteno	330	2014A-0613	David Rodriguez	57 57	2019A-0911	Jeffrey Cooke	9
	Douglas P Finkbeiner	324	2019A-0101	Patrick M Hartigan	57	2020B-0053	Dillon Brout	8

Table 3 continued

Table 3 (continued)

Prop.ID	PI	$N_{ m exp}$	Prop.ID	PI	$N_{ m exp}$	Prop.ID	PI	$N_{ m exp}$
2014A-0412	Armin Rest	303	2019B-0910	Yue Shen	55	2013A-0455	Scott Sheppard	7
2013A-0719	Abhijit Saha	291	2017B-0163	Prashin Jethwa	54	2012B-0416	David Nidever	7
2019A-0205	Daniel Goldstein	290	2013A-0612	Yun-Kyeong Sheen	53	2017B-0199	Anton Koekemoer	7
2018A-0215	Jeffrey Carlin	289	2017A-0913	Luidhy Santana da Silva	51	2013A-0609	Douglas P Geisler	7
2014A-0620	Andrew Casey	287	2014A-0610	Matthew Taylor	50	2020B-0021	Haojing Yan	7
2015A-0306	Eduardo Balbinot	280	2015A-0371	Armin Rest	50	2017A-0366	Sangeeta Malhotra	7
2014B-0244	Anja von der Linden	280	2016B-0173	Anton Koekemoer	49	2017B-0253	Jeffrey Carlin	6
2019B-0371	Marcelle Soares-Santos	280	2017A-0909	Jeffrey Cooke	49	2014A-0399	Christopher Johnson	6
2016B-0905	Helmut Jerjen	276	2015A-0615	Brendan McMonigal	49	2015B-0314	Brad Tucker	5
2017A-0914	Grant Tremblay	274	2017A-0308	Annalisa Calamida	48	2020A-0415	Armin Rest	5
2016A-0397	Anja von der Linden	263	2017A-0389	Armin Rest	48	2014A-0640	Amy Mainzer	5
2017A-0060	Denija Crnojevic	261	2014B-0609	Roberto R Munoz	47	2014B-0071	Sarah Sonnett	5
2017A-0281	Monika D Soraisam	256	2018A-0912	Attila Popping	45	2015B-0607	Jeffrey Cooke	5
2017A-0916	Julio Carballo-Bello	242	2021A-0246		44	2019B-1012	Jeffrey Cooke	5
2020A-0335	Lifan Wang	242	2020A-0238	Clara Martinez-Vazquez	43	2017B-0307	Scott Sheppard	4
2017B-0907	Ricardo Munoz	228	2019A-0325	Clara Martinez-Vazquez	43	2012B-0451	Scott Sheppard	4
2015A-0630	Thomas H Puzia	218	2020A-0142	Tom Shanks	42	2015A-0614	Jeffrey Cooke	4
2016A-0327	Douglas P Finkbeiner	216	2014B-0608	Yara Jaffe	41	2013B-0325	Kathy Vivas	4
2018B-0122	Armin Rest	213	2017A-0911	Ana Chies Santos	39	2020B-0288	Alexie Leauthaud	4
2012B-0569	Lori Allen	206	2020A-0909	Patricia Arevalo	39	2012B-0624	Aaron Robotham	4
2019A-0915	Jose Pena	191	2016A-0004	Ana Bonaca	38	2012B-3002	Josh Bloom	4
2015A-0619	Thiago Goncalves	186	2014A-0157	Andrej Favia	38	2015B-0603	Leopoldo Infante	4
2014A-0327	Armin Rest	183	2012B-0363	Josh Bloom	38	2015A-0177	Cristian Eduard Rusu	3
2018A-0059	Herve Bouy	182	2016A-0068	Thomas Deboer	38	2012B-0448	Paul Thorman	3
2015A-0163	Carl J Grillmair	179	2015B-0191	Sarah Rice	37	2014B-0378	Armin Rest	3
2018A-0911	Francisco Forster	174	2014A-0255	Anton Koekemoer	35	2013A-0613	Ricardo Munoz	3
2017B-0110	Edo Berger	174	2017B-0951	Kathy Vivas	35	2013A-0400	Josh Bloom	3
2016B-0910	Thomas H Puzia	174	2016B-0904	Igor Andreoni	33	2013A-0616	Geraint Lewis	2
2015A-0130	Denija Crnojevic	173	2019A-0060	Herve Bouy	33	2020A-0913	Jeremy Mould	2
2016B-0279	Douglas P Finkbeiner	170	2021A-0113	Melissa L Graham	33	2016A-0610	Leopoldo Infante	2
2013B-0614	Ricardo Munoz	167	2018A-0907	Ricardo Munoz	32	2013A-0608	Ricardo Demarco	2
2015A-0121	Anja von der Linden	160	2019B-1004	Julio Chaname	32	2014A-0191	Hendrik Hildebrandt	2
2019A-0917	Paulo Lopes	159	2012B-0506	Daniel D Kelson	32	2017B-0905	Jeremy Mould	2
2018A-0369	Armin Rest	156	2015A-0632	Cesar Briceno	31	2015B-0250	Jonathan Hargis	1
2017A-0918	Alexandra Yip	155	2013B-0531	Eric Mamajek	31	2012B-3016	Scott Sheppard	1
2013A-0611	Dougal Mackey	142	2018B-0904	Lee Splitter	30	2012B-0617	Robert I Hynes	1
2014B-0146	Mark Sullivan	141	2014A-0623	Ken Freeman	30	2013A-0610	Mario Hamuy	1
2014A-0256	Kathleen Eckert	136	2013A-0723	Eric Mamajek	28	2016A-0386	Sangeeta Malhotra	1
2015A-0205	Eric Mamajek	135	2019A-0315	Matthew Penny	28	2017A-0917	Franz Bauer	1
2014A-0321	Marla Geha	133	2013A-2101	Alistair Walker	28	2013B-0502	Ian Dell'Antonio	1
2017B-0904	Paulo Lopes	133	2015A-0107	Claudia Belardi	28	2013B-0613	Roberto R Munoz	1
2019A-0913	Julio Carballo-Bello	133	2013B-0438	Casey Papovich	26	2015A-0059	Sarah Sonnett	1
2015A-0397	Armin Rest	126	2013A-0621	Matias Gomez	25	2013A-0704	Matt A Wood	1
2019B-1010	Jose Pena	123	2016A-0104	Mark Sullivan	24			

Note—Programs are ordered by the number of exposures contributed. The largest single contributors to the DELVE DR2 data set are DES, DECaLS and the DELVE program itself. Programs with no principal investigator (PI) listed are generally Target-of-Opportunity (ToO) or multi-PI programs.

B. DELVE DR2 TABLES

The DELVE DR2 catalog data are accessible through the DELVE_DR2.0BJECTS table hosted by the Astro Data Lab. This table includes the photometric properties assembled from a catalog-level co-add of the individual single-epoch measurements. The table columns are described in Table 4. In addition, cross-matches between objects in the DELVE DR2 catalog and objects within 1".5 from external catalogs are provided in individual tables:

- DELVE_DR2.X1P5_OBJECTS_ALLWISE_SOURCE AllWISE (Cutri et al. 2021)
- DELVE_DR2.X1P5_OBJECTS_GAIA_EDR3_GAIA_SOURCE Gaia EDR3 (Gaia Collaboration 2021)
- DELVE_DR2.X1P5_OBJECTS_NSC_DR2_OBJECT NSC DR2 (Nidever et al. 2021)
- DELVE_DR2.X1P5_OBJECTS_SDSS_DR16_SPECOBJ SDSS DR16 (Ahumada et al. 2020)
- DELVE_DR2.X1P5_OBJECTS_UNWISE_DR1_OBJECT unWISE_DR1 (Schlafly et al. 2019)

A template for the columns in these tables are described in Table 5. The schema for these tables are also described in detail on the Astro Data Lab website.

C. DEPTH

This appendix includes sky maps showing variations in the S/N=5 depth of DELVE DR2 in the g, r, i, z bands. The S/N=5 depth was derived from the magnitude at which the median magnitude uncertainty was $\delta m = 0.2171$ mag (Section 4.6). These values were derived in $\sim 12 \, \mathrm{arcmin^2}$ HEALPix pixels (nside = 1024) and are shown in Figure 10.

 $\textbf{Table 4. DELVE.DR2_MAIN table description: } 2,500,247,752 \ \ rows; \ 126 \ columns$

Column Name	Description	Columns
QUICK_OBJECT_ID	Unique identifier for each object	1
RA	Right ascension derived from the median position of each detection (deg)	1
DEC	Declination derived from the median position of each detection (deg)	1
GLON	Galactic longitude derived from RA,DEC (deg)	1
GLAT	Galactic latitude derived from RA,DEC (deg)	1
ELON	Ecliptic longitude derived from RA,DEC (deg)	1
ELAT	Ecliptic latitude derived from RA,DEC (deg)	1
$A_{IMAGE_{G,R,I,Z}}$	Semi-major axis of adaptive aperture in image coordinates (pix)	4
$B_{IMAGE_{G,R,I,Z}}$	Semi-minor axis of adaptive aperture in image coordinates (pix)	4
$CCDNUM_{G,R,I,Z}$	CCD number for best exposure in each band	4
$CLASS_STAR_\{G,R,I,Z\}$	Neural-network-based star-galaxy classifier (see SourceExtractor manual for details)	4
EBV	E(B-V) value at the object location interpolated from the map of Schlegel et al. (1998)	1
$EXPNUM_{G,R,I,Z}$	Exposure number for best exposure in each band	4
$\text{EXPTIME}_{G,R,I,Z}$	Shutter-open exposure time for best exposure in each band	4
EXTENDED_CLASS_{G,R,I,Z}	Spread-model-based morphology class (see Section 4.7)	4
E.11 E.18 E.B = 0 E.188 = (0,11,1,2)	-9 unknown, 0 high-confidence star, 1 likely star, 2 likely galaxy, 3 high-confidence galaxy	-
EXTINCTION_{G,R,I,Z}	Interstellar extinction calculated from Schlegel et al. (1998). Subtract these columns from	4
27111(01101(-(0,10,1,2)	the magnitude columns to correct for extinction (see Section 3).	-
$FLAGS_{G,R,I,Z}$	SourceExtractor flags for the best detection in each band	4
HPX2048	HEALPix index for each object in RING format at resolution nside = 2048	1
HTM9	HTM Level-9 index	1
MAG_AUTO_{G,R,I,Z}	Automatic aperture magnitude derived from the best exposure in each band	4
MAGERR_AUTO_{G,R,I,Z}	Automatic aperture magnitude uncertainty derived from the best exposure in each band	4
MAG_PSF_{G,R,I,Z}	PSF magnitude derived from the best exposure in each band	4
MAGERR_PSF_{G,R,I,Z}	PSF magnitude uncertainty derived from the best exposure in each band	4
MJD_OBS	Median Modified Julian Date of the observations that were used to determine the astrometric position	1
	Number of single-epoch detections for this object	4
NEPOCHS_{G,R,I,Z} NEST4096	HEALPix index for each object in NEST format at resolution nside = 4096	1
	·	1
RANDOM_ID	Random ID in the range 0.0 to 100.0 for subsampling	_
RING256	HEALPix index for each object in RING format at resolution nside = 256	1
SPREAD_MODEL_{G,R,I,Z}	Likelihood-based star–galaxy classifier (Desai et al. 2012)	4
SPREADERR_MODEL_{G,R,I,Z}	Likelihood-based star-galaxy classifier uncertainty (Desai et al. 2012)	4
T_EFF_{G,R,I,Z}	Effective exposure time scale factor for best exposure in each band (Neilsen et al. 2016)	4
THETA_IMAGE_{G,R,I,Z}	Position angle of automatic aperture in image coordinates (deg)	4
$WAVG_FLAGS_\{G,R,I,Z\}$	OR of SourceExtractor flags from all detections in each band	4
WAVG_MAG_AUTO_{G,R,I,Z}	Weighted average of automatic aperture magnitude measurements in each band	4
$WAVG_MAGERR_AUTO_\{G,R,I,Z\}$	Sum in quadrature of the automatic aperture magnitude uncertainties in each band	4
WAVG_MAGRMS_AUTO_{G,R,I,Z}	Unbiased weighted standard deviation of the automatic aperture magnitude in each band	4
$WAVG_MAG_PSF_\{G,R,I,Z\}$	Weighted average of PSF magnitude measurements in each band	4
WAVG_MAGERR_PSF_{G,R,I,Z}	Sum in quadrature of the PSF magnitude uncertainties in each band	4
$WAVG_MAGRMS_PSF_\{G,R,I,Z\}$	Unbiased weighted standard deviation of the PSF magnitude in each band	4
$WAVG_SPREAD_MODEL_\{G,R,I,Z\}$	Weighted average spread model in each band	4
$WAVG_SPREADERR_MODEL_\{G,R,I,Z\}$	Sum in quadrature of the spread model uncertainties in each band	4
WAVG_SPREADRMS_MODEL_{G,R,I,Z}	Unbiased weighted standard deviation of SPREAD_MODEL in each band	4

 ${\bf Table~5.} \quad {\bf Crossmatch~tables~between~DELVE~DR2~and~external~catalogs}.$

Column Name	Description	Columns
DEC1	Declination from DELVE DR2 (deg)	1
DEC2	Declination from external catalog (deg)	1
DISTANCE	Angular separation between RA1,DEC1 and RA2,DEC2 (arcsec)	1
ID1	ID in DELVE DR2 (QUICK_OBJECT_ID)	1
ID2	ID in external catalog (SOURCE_ID)	1
RA1	Right ascension from DELVE DR2 (deg)	1
RA2	Right ascension from external catalog (deg)	1

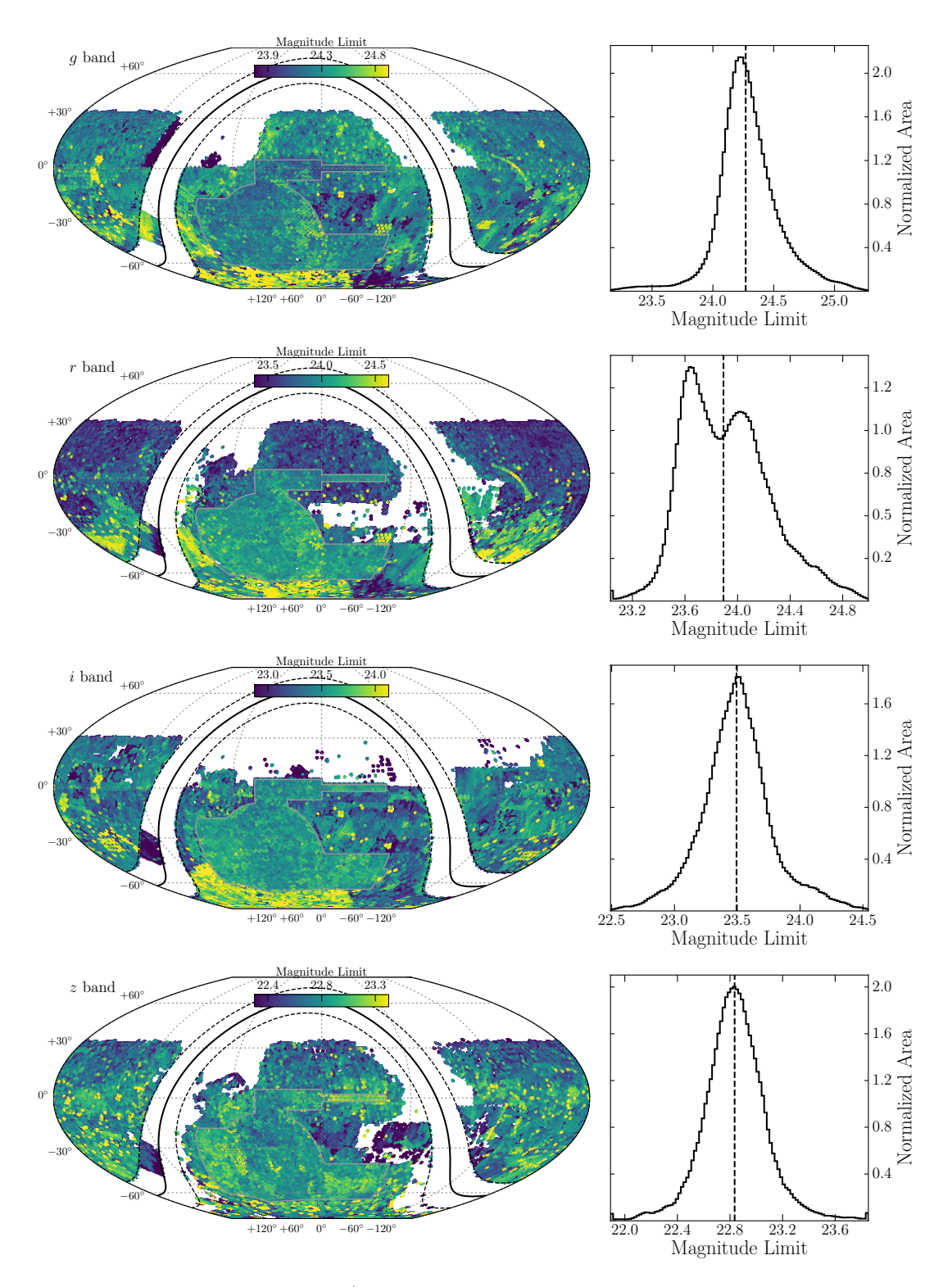


Figure 10. Sky maps and histograms of the S/N=5 magnitude limit computed from the statistical uncertainty in MAG_PSF. Dashed vertical lines indicate the median depth quoted in Table 1. Sky maps are plotted using an equal-area McBryde–Thomas flat polar quartic projection in celestial equatorial coordinates.

REFERENCES

- Ahumada, R., Prieto, C. A., Almeida, A., et al. 2020, ApJS, 249, 3, arXiv:1912.02905
- Aihara, H., AlSayyad, Y., Ando, M., et al. 2022, PASJ, 74, 247, arXiv:2108.13045
- Astropy Collaboration. 2018, AJ, 156, 123, arXiv:1801.02634
- Bernstein, G. M., Abbott, T. M. C., Armstrong, R., et al. 2018, PASP, 130, 054501, arXiv:1710.10943
- Bertin, E. 2006, in Astronomical Society of the Pacific
 Conference Series, Vol. 351, Astronomical Data Analysis
 Software and Systems XV, ed. C. Gabriel, C. Arviset,
 D. Ponz, & S. Enrique, 112
- Bertin, E. 2011, in Astronomical Society of the Pacific
 Conference Series, Vol. 442, Astronomical Data Analysis
 Software and Systems XX, ed. I. N. Evans, A. Accomazzi,
 D. J. Mink, & A. H. Rots, San Francisco, CA, 435
- Bertin, E. & Arnouts, S. 1996, A&AS, 117, 393
- Burke, D. L., Rykoff, E. S., Allam, S., et al. 2018, AJ, 155, 41, arXiv:1706.01542
- Cerny, W., Pace, A. B., Drlica-Wagner, A., et al. 2021a, ApJ, 910, 18, arXiv:2009.08550
- Cerny, W., Pace, A. B., Drlica-Wagner, A., et al. 2021b, ApJL, 920, L44, arXiv:2107.09080
- Cerny, W., Simon, J. D., Li, T. S., et al. 2022, arXiv e-prints, arXiv:2203.11788, arXiv:2203.11788
- Chambers, K. C., Magnier, E. A., Metcalfe, N., et al. 2016, ArXiv e-prints, arXiv:1612.05560
- Coupon, J., Kilbinger, M., McCracken, H. J., et al. 2012, A&A, 542, A5, arXiv:1107.0616
- Cutri, R. M., Wright, E. L., Conrow, T., et al. 2021, VizieR Online Data Catalog, II/328
- DES Collaboration. 2005, arXiv:astro-ph/0510346
- DES Collaboration. 2018, ApJS, 239, 18, arXiv:1801.03181
- DES Collaboration. 2016, MNRAS, 460, 1270, arXiv:1601.00329
- DES Collaboration. 2021, ApJS, 255, 20, arXiv:2101.05765
- Desai, S., Armstrong, R., Mohr, J. J., et al. 2012, ApJ, 757, 83, arXiv:1204.1210
- Dey, A., Schlegel, D. J., Lang, D., et al. 2019, AJ, 157, 168, arXiv:1804.08657
- Drlica-Wagner, A., Sevilla-Noarbe, I., Rykoff, E. S., et al. 2018, ApJS, 235, 33, arXiv:1708.01531
- Drlica-Wagner, A., Carlin, J. L., Nidever, D. L., et al. 2021, ApJS, 256, 2, arXiv:2103.07476
- Ferguson, P. S., Shipp, N., Drlica-Wagner, A., et al. 2022, AJ, 163, 18, arXiv:2104.11755

- Fitzpatrick, M. J., Graham, M. J., Mighell, K. J., et al.
 2016, in Society of Photo-Optical Instrumentation
 Engineers (SPIE) Conference Series, Vol. 9913, Software
 and Cyberinfrastructure for Astronomy IV, ed.
 G. Chiozzi & J. C. Guzman, 99130L
- Flaugher, B., Diehl, H. T., Honscheid, K., et al. 2015, AJ, 150, 150, arXiv:1504.02900
- Gaia Collaboration. 2018, A&A, 616, A14, arXiv:1804.09377
- Gaia Collaboration. 2021, A&A, 649, A1, arXiv:2012.01533
 Gilbank, D. G., Gladders, M. D., Yee, H. K. C., & Hsieh,
 B. C. 2011, AJ, 141, 94, arXiv:1012.3470
- Górski, K. M., Hivon, E., Banday, A. J., et al. 2005, ApJ, 622, 759, astro-ph/0409513
- Harris, C. R., Millman, K. J., van der Walt, S. J., et al. 2020, Nature, 585, 357, arXiv:2006.10256
- High, F. W., Stubbs, C. W., Rest, A., Stalder, B., & Challis, P. 2009, AJ, 138, 110, arXiv:0903.5302
- Hunter, J. D. 2007, CSE, 9, 90
- Ivezić, Ž., Lupton, R. H., Schlegel, D., et al. 2004, Astronomische Nachrichten, 325, 583, astro-ph/0410195
- Jethwa, P., Erkal, D., & Belokurov, V. 2018, MNRAS, 473, 2060, arXiv:1612.07834
- Kelly, P. L., von der Linden, A., Applegate, D. E., et al. 2014, MNRAS, 439, 28, arXiv:1208.0602
- Kent, S. M. 2013, FERMILAB-SLIDES-20-114-SCD
- MacDonald, E. C., Allen, P., Dalton, G., et al. 2004, MNRAS, 352, 1255, astro-ph/0405208
- Martínez-Vázquez, C. E., Cerny, W., Vivas, A. K., et al. 2021, AJ, 162, 253, arXiv:2107.05688
- Mau, S., Cerny, W., Pace, A. B., et al. 2020, ApJ, 890, 136, arXiv:1912.03301
- Morganson, E., Gruendl, R. A., Menanteau, F., et al. 2018, PASP, 130, 074501, arXiv:1801.03177
- Neilsen, E., Bernstein, G., Gruendl, R., & Kent, S. 2016, "Limiting magnitude, τ , T_{eff} , and image quality in DES Year 1", Tech. Rep. FERMILAB-TM-2610-AE-CD, Fermi National Accelerator Laboratory
- Nidever, D. L., Dey, A., Olsen, K., et al. 2018, AJ, 156, 131, arXiv:1801.01885
- Nidever, D. L., Dey, A., Fasbender, K., et al. 2021, AJ, 161, 192, arXiv:2011.08868
- Nikutta, R., Fitzpatrick, M., Scott, A., & Weaver, B. 2020, Astronomy and Computing, 33, 100411
- Oke, J. B. & Gunn, J. E. 1983, ApJ, 266, 713
- Pogson, N. 1856, MNRAS, 17, 12
- Rykoff, E. S., Rozo, E., & Keisler, R. 2015, arXiv e-prints, arXiv:1509.00870, arXiv:1509.00870

- Schlafly, E. F. & Finkbeiner, D. P. 2011, ApJ, 737, 103, arXiv:1012.4804
- Schlafly, E. F., Meisner, A. M., & Green, G. M. 2019, ApJS, 240, 30, arXiv:1901.03337
- Schlegel, D. J., Finkbeiner, D. P., & Davis, M. 1998, ApJ, 500, 525, astro-ph/9710327
- Sevilla-Noarbe, I., Bechtol, K., Carrasco Kind, M., et al. 2021, ApJS, 254, 24, arXiv:2011.03407
- Skrutskie, M. F., Cutri, R. M., Stiening, R., et al. 2006, AJ, 131, 1163
- Tanoglidis, D., Ćiprijanović, A., Drlica-Wagner, A., et al. 2022, Astronomy and Computing, 39, 100580, arXiv:2109.08246
- Tonry, J. L., Denneau, L., Flewelling, H., et al. 2018, ApJ, 867, 105, arXiv:1809.09157

- Valdes, F., Gruendl, R., & DES Project. 2014, in
 Astronomical Society of the Pacific Conference Series,
 Vol. 485, Astronomical Data Analysis Software and
 Systems XXIII, ed. N. Manset & P. Forshay, 379
- Virtanen, P., Gommers, R., Oliphant, T. E., et al. 2020, Nature Methods, 17, 261, arXiv:1907.10121
- Wolf, C., Onken, C. A., Luvaul, L. C., et al. 2018, PASA, 35, e010, arXiv:1801.07834
- York, D. G., Adelman, J., Anderson, Jr., J. E., et al. 2000, AJ, 120, 1579, astro-ph/0006396
- Zonca, A., Singer, L., Lenz, D., et al. 2019, JOSS, 4, 1298